



UPPSALA
UNIVERSITET



UNIVERSITY
OF OULU

X-ray Absorption and Fragmentation as Initial Steps of Radiation Damage in Free Organic Molecules and Nanoparticles

ABDUL RAHMAN ABID

REPORT SERIES IN PHYSICAL SCIENCES

Report No. 139 (2021)

University of Oulu • Uppsala University

X-ray Absorption and Fragmentation as Initial Steps of Radiation Damage in Free Organic Molecules and Nanoparticles

ABDUL RAHMAN ABID

*Nano and Molecular Systems Research Unit (NANOMO)
Faculty of Science, University of Oulu
FINLAND*

*Molecular and Condensed Matter Physics
Department of Physics and Astronomy, Uppsala University
SWEDEN*

Academic Dissertation to be presented with the assent of the Faculty of Science, University of Oulu, Finland and Department of Physics and Astronomy, Uppsala University, Sweden for public discussion in the Auditorium L2, on April 7th, 2021, at 11 o'clock (EEST) morning.

Supervisors:

Assoc. Prof. Minna Patanen, University of Oulu, Finland

Prof. Olle Björneholm, Uppsala University, Sweden

Adj. Prof. Juha Nikkinen, University of Oulu, Finland

Opponent:

Dr. Laurent Nahon, Synchrotron SOLEIL, Saint-Aubin, France

Reviewers:

Dr. Joachim Schulz, EuXFEL, Hamburg, Germany

Dr. Paola Bolognesi, CNR-ISM, Rome, Italy

Custos:

Prof. Marko Huttula, University of Oulu, Finland

Cover Design by Abdul Rahman Abid

ISBN 978-952-62-2884-6 (Printed)

ISBN 978-952-62-2885-3 (PDF)

ISSN 1239-4327

PunaMusta Oy

Oulu 2021/Uppsala 2021

*“No two things have been combined together
better than **knowledge** and **patience**.”*
-Muhammad (PBUH)

Abid, Abdul Rahman: X-ray Absorption and Fragmentation as Initial Steps of Radiation Damage in Free Organic Molecules and Nanoparticles

Nano and Molecular Systems Research Unit, Faculty of Science
P.O. Box 3000
FIN-90014 University of Oulu
FINLAND

Molecular and Condensed Matter Physics
Department of Physics and Astronomy
Box 516, Uppsala University
SE-751 20 Uppsala
SWEDEN

Abstract

Understanding the molecular radiation damage is crucial in radiobiology, molecular physics, and atmospheric science. In this thesis, the initial steps of radiation damage of anhydrous gas-phase molecules and hydrated nanoparticles were studied using synchrotron radiation based electron-ion coincidence spectroscopy and X-ray absorption spectroscopy under vacuum conditions. Electron - ion coincidence spectroscopy was used to study the photofragmentation and molecular dynamics of the isolated gas-phase molecules. In addition to the photofragmentation of the gas-phase molecules, the effect of the initial ionization site, initial molecular geometry, and the intramolecular chemical environment has been studied. In avobenzene, core ionization leads to massive fragmentation, with a slight site-selectivity concerning fragment production. In ortho-aminobenzoic acid, core ionization leads to the production of a hydronium ion, indicating that the importance of functional group's position for double intramolecular hydrogen transfer. X-ray absorption spectroscopy was used to probe hydrated nanoparticles prepared at different relative humidities. In hydrated inorganic and mixed inorganic-organic nanoparticles, water is present in a liquid-like state. With different ranges of relative humidity, the primary hydration layers of the hydrated nanoparticles stays the same. In mixed nanoparticles, there is evidence for interaction between the included organic biomolecule with the inorganic and/or water molecules.

Key words: Coincidence spectroscopy, PEPI(PI)CO, electron spectroscopy, X-ray absorption spectroscopy, mass spectrometry, photodissociation, gas-phase, liquids, nanoparticles, charge transfer, synchrotron radiation

**Abid, Abdul Rahman: Röntgenabsorptio ja fragmentaatio säteilyvaurioiden ensimmäisinä vaiheina vapaissa orgaanisissa molekyyli-
ssä ja nanopartikkeleissa**

Nano and Molecular Systems Research Unit, Faculty of Science
P.O. Box 3000
FIN-90014 University of Oulu
FINLAND

Molecular and Condensed Matter Physics
Department of Physics and Astronomy
Box 516, Uppsala University
SE-751 20 Uppsala
SWEDEN

Abstrakti

Molekyyllitasolla tapahtuvien säteilyvaurioiden ymmärrys on erittäin tärkeää säteilybiologiassa, molekyyllifysiikassa ja ilmakehätieteissä. Tässä työssä on tutkittu tyhjiöolosuhteissa säteilyvaurioiden alkuaskeleita vedettömissä kaasumaisissa molekyyli- ja vettä sisältävissä nanohiukkasissa käyttäen synkrotronisäteilypohjaista elektroni-ionikoinssidenssispektroskopiaa ja röntgenabsorptiospektroskopiaa. Elektroni-ionikoinssidenssispektroskopiolla tutkittiin säteilyn aikaansaamaa hajoamista ja molekyylidynamiikkaa eristetyissä kaasumolekyyli- ja vettä sisältävissä nanohiukkasissa. Tämän lisäksi tutkittiin, kuinka ensimmäisen ionisaatiota-
pahtuman paikka, molekyylin geometria ja molekyylin sisäinen kemiallinen ympäristö vaikuttaa näihin prosesseihin. Avobentsonimolekyylin sisäkuoren ionisaatio johtaa molekyylin hajoamiseen lukuisiksi eri hajoamistuotteiksi, ja hajoamistuotteiden saannin todettiin riippuvan vain vähän ionisoidusta sisäkuoresta. Orto-aminobentsoehapossa sisäkuoren ionisaation havaittiin tuottavan kahden vedyn siirtymisen vaativaa hydroniumionia, ja tuoton havaittiin riippuvan funktionaalisten ryhmien keskinäisestä paikasta. Röntgenabsorptiospektroskopiaa hyödynnettiin eri suhteellisissa ilmakehätieteissä valmistettujen nanohiukkasten tutkimuksessa. Näissä epäorgaanisissa ja saostetuissa orgaanisissa-epäorgaanisissa nanohiukkasissa veden havaittiin olevan nesteenkaltaisessa olomuodossa. Saostetuissa nanohiukkasissa nähtiin myös merkkejä orgaanisen biomolekyylin ja epäorgaanisen ja/tai veden välisestä vuorovaikutuksesta.

Avainsanat: Koinssidenssispektroskopia, PEPICO, elektronispektroskopia, röntgenabsorptiospektroskopia, massaspektroskopia, fotodissosiaatio, kaasufaasi, neste, nanohiukkaset, varauksen siirto, synkrotronisäteily

Abid, Abdul Rahman: Röntgenabsorption och fragmentering som initiala steg för strålskador i fria organiska molekyler och nanopartiklar

Nano and Molecular Systems Research Unit
Naturvetenskapliga fakulteten
Box 3000, FIN-90014 University of Oulu
FINLAND

Kemisk och biomolekylär fysik
Institutionen för fysik och astronomi
Box 516, Uppsala universitet
SE-751 20 Uppsala
SVERIGE

Sammanfattning

Förståelse av molekulära strålningsskador är avgörande inom radiobiologi, molekulär fysik och atmosfärsvetenskap. I denna avhandling studerades strålningsskadornas inledande steg hos gasfasmolekyler och hydratiserade nanopartiklar med hjälp av synkrotronstrålningsbaserad elektron-jon-koincidensspektroskopi och röntgenabsorptionsspektroskopi under vakuumförhållanden. Elektron-jon-koincidensspektroskopi användes för att studera fotofragmentering och molekulär dynamik hos de isolerade gasfasmolekylerna. Förutom fotofragmenteringen av gasfasmolekylerna har effekten av den initiala joniseringsplatsen i molekylen, den initiala molekulära geometrin och den intramolekulära kemiska miljön studerats. I avobenzon leder innerskalsjonisering till massiv fragmentering med liten platsselektivitet beträffande fragmentproduktion. I orto-aminobensoesyra leder innerskalsjonisering till produktion av en hydroniumjon, vilket pekar på vikten av funktionella grupper position för sådan dubbel intramolekulär väteöverföring. Röntgenabsorptionsspektroskopi användes för att studera hydratiserade nanopartiklar framställda vid varierande relativa fuktighet. I hydratiserade inorganiska och blandade inorganiska-organiska nanopartiklar finns vatten i vätskeformigt tillstånd. De primära hydratiseringsskalen i de hydratiserade nanopartiklarna opåverkade av de olika relativa fuktighetsnivåerna. I blandade nanopartiklar finns det bevis för växelverkan mellan de inkluderade organiska biomolekylerna och de inorganiska jonerna och/eller vattenmolekylerna.

Nyckelord: koincidensspektroskopi, PEPI(PI)CO, elektronspektroskopi, röntgenabsorptionsspektroskopi, masspektrometri, fotodissociation, gasfas, vätskor, nanopartiklar, laddningsöverföring, synkrotronstrålning

Acknowledgments

The present work was carried out in the Nano and Molecular (NANOMO) Research Unit of the University of Oulu, Finland, and Molecular and Condensed Matter Physics of the Uppsala University, Sweden. This project has received funding from the European Union’s Horizon 2020 research and innovation programme “*I4Future*” under the Marie Skłodowska-Curie grant agreement (No. 713606). This project also received funding from Väisälä Fund, Finnish Academy of Science and Letters to finalize my doctoral thesis. This project was also granted travel funding from CALIPSOPlus from the EU framework programme for research and innovation Horizon 2020 (Grant agreement no. 730872), the Magnus Ehrnrooth Foundation, Finland, and the University of Oulu Graduate School (UniOGS) for several beamtimes and research visits.

I want to thank my supervisors, Assoc. Prof. Minna Patanen, Prof. Olle Björneholm, and Adj. Prof. Juha Nikkinen guided me through the challenging time of the doctoral research and have all the patience and understanding required while working with me. Especially, Minna and Olle, I know that such a dedication to supervision and support is rare. I learned many things from the discussions we have during our meetings. A special thanks to the NANOMO research unit head, Prof. Marko Huttula, for his support, who facilitated me throughout my doctoral research. I am also grateful to Profs. Ville-Veikko Telkki and Mika Nieminen as members of my doctoral follow-up group and guidance during the follow-up meetings.

This work is a result of intensive teamwork, so I would like to thank my colleagues Nacer Boudjemia, Eetu Pelimanni, Maximilian Reinhardt, Georgia Michailoudi, Paavo Turunen, and Tuomas Löytynoja for their valuable discussions and assistance. We did many discussions not only related to the work but anyway interesting and piquant at the intellectual level. I also appreciate the mental support which I got from the other members of the NANOMO research unit. I want to thank Drs. Conny Sæthe, Takashi Tokushima, Victor Ekholm, and Nial Wassdahl for the facilitation and support during research visits at VERITAS Beamline, MAX IV Laboratory. As the work was based on experimental activities, none of it would have been possible without the support of beamline staff Drs. Antti Kivimäki, Kirill Chernenko, Gunnar Öhrwall, and Aleksandar Milosavljević from MAX IV and SOLEIL. I am thankful to Drs. Joachim Schulz and Paola Bolognesi

for their helpful role as pre-examiners for this thesis. Thanks to all I4Future family, It was a pleasure to meet you all!

Even though doctoral studies have been challenging, it is only a small fraction of the bigger life journey during which I have continuously received support and appreciation from my family. Thanks to my parents, Asghar Ali and Khursheed Begum, for giving me their full support, understanding, and prayers to freely follow my aspirations. I also want to thank my brothers and sisters, Nadeem, Naeem, Kalsoom, Kausar, and Ansa, for supporting me in several phases of my life. Last but not least, I want to thank my beloved wife, Dr. Somia, for always creating the best environments for me so I can follow my dreams and our daughter Samavia for providing the critical work-life balance and so much bliss to our life in Finland.

Oulu, February 2021 Abdul Rahman Abid

LIST OF ORIGINAL PAPERS

The present thesis contains an introductory part and the following papers which will be referred in the text by their Roman numbers.

- I. **A. R. Abid**, E. Pelimanni, M. Reinhardt, N. Boudjemia, A. Kivimäki, M. Huttula, O. Björneholm, and M. Patanen: *Electron-ion coincidence spectroscopy of a large organic molecule: Photofragmentation of avobenzene after valence and core ionisation* J. Phys. B: At. Mol. Opt. Phys. **53**, (2020) 244001. (DOI: [10.1088/1361-6455/abc228](https://doi.org/10.1088/1361-6455/abc228))
- II. **A. R. Abid**, O. Veteläinen, N. Boudjemia, E. Pelimanni, A. Kivimäki, M. Alatalo, M. Huttula, O. Björneholm, and M. Patanen: *Isomer-Dependent Formation of H_3O^+ via Intramolecular Double Hydrogen Transfer in Aminobenzoic Acid* (2021). (Manuscript)
- III. **A. R. Abid**, M. Reinhardt, N. Boudjemia, E. Pelimanni, A. R. Milosavljević, C.-M. Saak, M. Huttula, O. Björneholm, and M. Patanen: *The effect of relative humidity on $CaCl_2$ nanoparticles studied by soft X-ray absorption spectroscopy* RSC Adv., **11**, (2021) 2103–2111. (DOI: [10.1039/D0RA08943E](https://doi.org/10.1039/D0RA08943E))

Comment on my own contribution:

All the papers for this doctoral dissertation are a result of teamwork. My doctoral research is the outcome of the continuous collaboration between the Oulu and Uppsala universities. Besides that, active collaboration with different large scale facilities, this experimental work would not have been possible.

To clarify my contributions to the publications. For all **Papers I-III**, I have been the main responsible person. The main responsibilities include planning and conducting experimental measurements, data collection, data treatment, and reporting the results.

List of Abbreviations

$h\nu$ Photon Energy

AES Auger Electron Spectroscopy

ALS Aerodynamics Lens

BO Born-Oppenheimer

CaCl_2 Calcium Chloride

cPGM Collimated Plane Grating Monochromator

EPU Elliptically Polarizing Undulator

HDA Hemispherical Deflection Analyzer

HOMO Highest Occupied Molecular Orbital

KE Kinetic Energy

KER Kinetic Energy Release

LCAO Linear Combinations of Atomic Orbitals

Linac Linear Accelerator

MCP Micro Channel Plate

MO Molecular Orbital

NEXAFS Near-Edge X-ray Absorption Fine Structure

PEPI(PI)CO Photoelectron, Photoion (Photoion) Coincidence Spectroscopy

PES Photoelectron Spectroscopy

PEY Partial Electron Yield

Phe Phenylalanine

RAD Resistive Anode Detector

RAS Resonant Auger Spectroscopy

RIXS Resonant Inelastic X-ray Scattering

SPF Short-Pulse-Facility

TEY Total Electron Yield

TOF Time-Of-Flight

TOF-MS Time-Of-Flight Mass Spectroscopy

UFD Ultrafast Dissociations

UPS Ultraviolet Photoelectron Spectroscopy

UV Ultraviolet

XAS X-ray Absorption Spectroscopy

XES X-ray Emission Spectroscopy

XPS X-ray Photoelectron Spectroscopy

XUV Extreme Ultraviolet

Contents

Abstract	i
Abstrakti	ii
Sammanfattning	iii
Acknowledgments	iv
List of original papers	vii
List of Abbreviations and Symbols	viii
Contents	xi
1 Introduction	1
2 Physical Foundation	5
2.1 Electronic Structure of Molecules	5
2.2 Potential Energy Curves	7
2.3 Light-Matter Interaction	9
2.3.1 Photoionization or Photoelectric Effect	9
2.3.2 Photoexcitation or Resonant Excitation	11
2.3.3 Fluorescence Decay	13
2.3.4 Spectroscopy Techniques	13
2.4 Molecular Dissociation and Fragmentation	14
3 Synchrotron Radiation and Sample Delivery Systems	19
3.1 Synchrotron Radiation	19
3.2 Characteristics of Synchrotron Radiation	21
3.2.1 Undulator Radiation	21
3.3 FinEstBeAMS Beamline at MAX IV	23
3.4 Sample Delivery Systems	25
3.4.1 Vapor Production	25
3.4.2 Free-Standing Nanoparticles Preparation	26
3.4.3 Liquid-Jet	28

CONTENTS

4	Spectroscopic Methods and Data Handling	31
4.1	Electron Spectroscopy	31
4.2	Time-of-Flight Mass Spectroscopy	34
4.3	X-ray Absorption Spectroscopy	37
4.4	Electron-Ion Coincidence Spectroscopy	38
4.4.1	PEPI(PI)CO Technique and Apparatus	39
4.4.2	CoboldPC Program Package	41
5	PEPIPICO Data Analysis	43
5.1	Basic PEPIPICO Data Handling	43
5.2	Dissociation Mechanisms	43
5.2.1	Two-Body Dissociation	44
5.2.2	Many-Body Dissociation	45
5.3	Pattern Slope Calculation	46
5.4	Challenges in Coincidence Spectroscopy Technique	50
6	Research Objectives and Results	53
6.1	Photofragmentation of Molecules - Papers I & II	53
6.1.1	Photofragmentation of Avobenzene - Paper I	53
6.1.2	Photofragmentation of Ortho-Aminobenzoic Acid - Paper II	58
6.2	XAS of Hydrated Nanoparticles - Paper III	59
7	Conclusion and Outlook	63
	Populärvetenskaplig sammanfattning	65
	Bibliography and References	69

Introduction

Radiation Damage: What and Where?

The importance of radiation-sensitive molecules in radiobiology and medicine is the primary motivation for these studies. For many decades, radiation damage caused by ionizing radiation (i.e. UV and X-rays) on biologically relevant molecules has been widely studied. These molecules also have several other applications like plastics, paints, and electronic devices, and moreover, they also have atmospheric relevance. Therefore, a microscopic understanding of these molecules, their electronic structure, and ionization processes is needed. Biomolecules often have several structural and conformational isomers, and one of the exciting perspectives in molecular physics is to study how properties vary between isomers. They also can have different molecular structures in gas-phase, in solutions, and as solids. The variety of interesting aspects in these biologically relevant molecules motivated us to study changes in the photofragmentation and photoabsorption processes connected to small structural variations in the molecules.

In this thesis, we studied organic and inorganic biologically relevant molecules. In **Papers I & II**, we performed gas-phase studies of *avobenzene* and *aminobenzoic acid* (organic) in different isomeric forms, as shown in figure 1.1. In **Paper III**, we generated hydrated nanoparticles of *calcium chloride* (CaCl_2) salt (inorganic) to study hydration properties. We also generated mixed inorganic-organic hydrated nanoparticles from CaCl_2 and *phenylalanine*¹ (Phe).

Seeing Through Soft X-ray Spectroscopic Methods

Molecular radiation damage can be studied using different spectroscopic methods like mass spectrometry[1], electron spectroscopy[1], X-ray absorption spectroscopy[2], and X-ray emission spectroscopy[3]. Upon photoioniza-

¹Chemical structure both in neutral and zwitterionic shown in figure 1.1

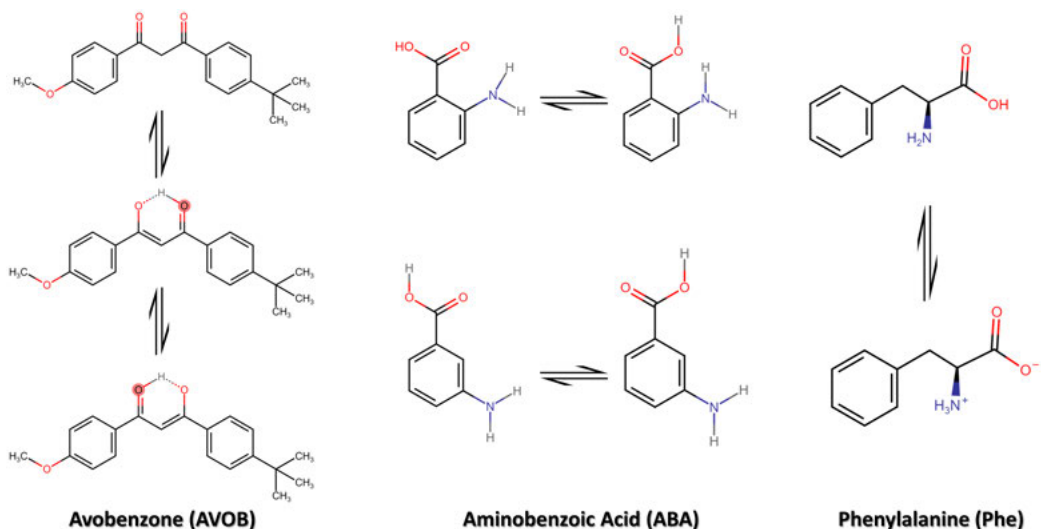


Figure 1.1: Chemical structure of organic molecules studied in this thesis with their isomers and conformers.

tion, one or more bond cleavages happen and lead to the fragmentation of the molecule. The created positive fragments are detected with the help of mass spectrometry. These fragments will give information about the possible sites of the bond break. Photoelectrons (and/or Auger electrons) are also ejected with different kinetic energy during photoionization. These electrons contain information about the electronic structure.

The amalgamation of *electron spectroscopy* and *mass spectrometry* allows electron detection to act as a timestamp for the starting point of ion detection. This technique is known as *electron-ion coincidence spectroscopy*. In this way, we can get the complete picture of the ionization processes in the system by recording several ionization events.

X-ray absorption spectroscopy (XAS) is a well established technique that provides element-specific information. Element-specific changes in XAS features give information on, in addition to the local atomic structure, lattice parameters, molecular orientation, density of states, the nature, orientation, and length of chemical bonds[4, 5]. This technique is capable to probe the solute's solvation environment like salts and biomolecules in water[6].

What We Did?

In this thesis, various spectroscopic methods were applied to study radiation damage in different radiation-sensitive biologically relevant molecules. All the experimental measurements were done using *synchrotron radiation*.

In **Papers I & II**, the studies consist of the photofragmentation of isolated gas-phase molecules with *electron-ion coincidence spectroscopy*. These studies help us to understand the fragmentation mechanisms and dynamics of the molecules. In **Paper III**, hydrated nanoparticles were studied with *X-ray absorption spectroscopy*. Different absorption edges were probed to learn about changes in the ions' and molecules' local structure and chemical environment. The presence and state of water within the nanoparticles were also investigated. From a broad perspective, these studies are beneficial for understanding radiation damage in molecules in anhydrous (isolated gas-phase) and hydrated (nanoparticles) form using synchrotron radiation. Moreover, the properties of nanoaerosols studied in **Paper III** are relevant for atmospheric science.

Structure of The Thesis

The introductory part of the thesis is structured as follows. *Chapter 2: Physical Foundation* explains the fundamental physical concepts lying behind our research work. *Chapter 3: Synchrotron Radiation and Sample Delivery Systems* describes the importance of synchrotron radiation and beamlines used for the measurements presented in **Papers I-III**. The sample delivery systems used in **Papers I-III** are also described in this chapter. *Chapter 4: Spectroscopic Methods and Data Handling* explains the spectroscopic methods used in **Papers I-III** and the post-experimental data handling. *Chapter 5: PEPICO Data Analysis* describes how sequential fragmentation can be analyzed through PEPICO spectroscopy and how the data analysis was done in **Papers I & II**. *Chapter 6: Research Objectives and Results* explains the main objectives behind our research and summarizes the results obtained. The last *Chapter 7: Conclusion and Outlook* concludes the introduction of the thesis and discusses some possible future research paths.

Physical Foundation

2.1 *Electronic Structure of Molecules*

Atoms consist of a densely packed positively charged nucleus having positively charged protons and neutral neutrons, around which negative electrons revolve, pictured as a hollow spherical assembly. In the atoms, the electrons are distributed in different orbitals. These electron orbitals are described by an electron wavefunction (ψ) written in terms of their spin and angular momenta. The wavefunctions can be obtained by solving the *Schrödinger equation*, which also yields the different energy states of an atom.

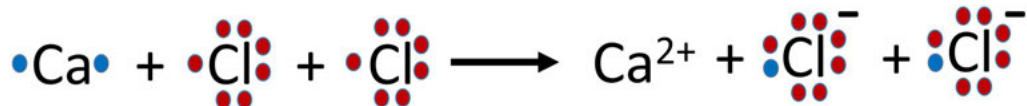
$$\hat{H}\psi = E\psi \quad (2.1)$$

In the equation 2.1, \hat{H} is a Hamiltonian, which operates on the wavefunction and gives eigenenergies (E) of the system [7–9]. The solution of the Schrödinger equation gives the set of quantum numbers related to atomic orbitals. These quantum numbers are the principal quantum number (n) having always a value $n \geq 1$, the azimuthal (angular) quantum number (l) having always a value $0 \leq l \leq n-1$, the magnetic quantum number (m_l) having always a value $-l \leq m_l \leq +l$, and the spin quantum number (m_s) having always a value $m_s = \pm 1/2$ [10]. The combination of these quantum numbers with different coupling schemes gives rise to different electron configurations and provides a description of the different quantum states.

In molecules, two or more atoms are interlinked with each other by ‘donating’ or ‘sharing’ electrons [11]. Donating or sharing electrons results in ionic or covalent bonds, respectively. The outermost valence electrons contribute to the bond formation process simplistically described in the *Lewis structure model*, as shown in figure 2.1 [12–17]. In the Lewis model, the electrons are allocated to a specific atom in the molecule, but in reality, that is not the case. The bonding theory is better described in *molecular orbital (MO) theory*, in which electrons are more delocalized. There are numbers of

molecular orbital theory descriptions available in the literature [11, 18–21]; here, a small introduction is given.

(a) Ionic Bonding



(b) Covalent Bonding

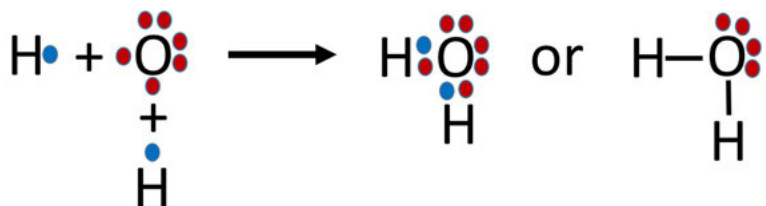


Figure 2.1: In the Lewis Model, (a) ionic bonding of a molecule consists of donating electrons and (b) covalent bonding of a molecule consists of sharing electrons.

Molecular orbitals can be described in terms of linear superpositions of atomic orbitals of every individual atom (*linear combination of atomic orbitals* (LCAO) approximation [21–24]).

$$\psi = \sum_i a_i \cdot \phi_i \quad (2.2)$$

In equation 2.2, ψ is a molecular orbital, a_i is a mixing coefficient describing the relative contribution of each atomic orbital, and ϕ_i is an atomic orbital. It is very useful to describe molecular orbitals by breaking them into atomic orbitals, since this will give us the information about the bonding properties of the molecule [25].

The schematics of a diatomic molecule are shown in figure 2.2, to explain how MOs are formed. When atomic orbitals on the different atoms overlap, two different distinct molecular orbitals are produced; one is a bonding combination indicated as σ_g . In the bonding state, molecular orbitals have maximum electron density between the nuclei, resembling the electron pair in the Lewis model. The other state called an anti-bonding states, indicated as σ_u^* , has a node in electron density between the nuclei. Therefore, we can say that the outdated Lewis model is replaced by the molecular orbital theory, which can describe how atoms bond into molecules (bonding state) or dissociate (anti-bonding state). The sign of the atomic orbitals is vital to

2.2 Potential Energy Curves

define the MOs' nature: with the same sign bonding MO form, but with opposite sign, anti-bonding MO will form. No interaction of atomic orbitals results in non-bonding MOs.

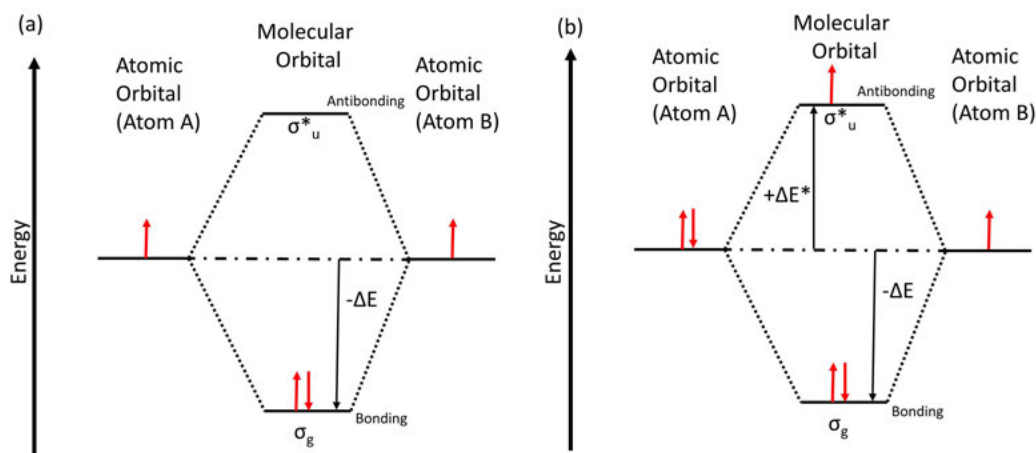


Figure 2.2: Schematic of the molecular orbitals of a molecule with both atoms having (a) the same number of electrons in valence orbitals (b) different number of electrons in valence orbitals.

The atomic orbitals are often categorized into valence and core orbitals. The valence orbitals are delocalized and contribute to the chemical bonding of the molecule. The core orbitals are localized and have higher binding energies, as shown in figure 2.3(b). The valence orbitals interact with other valence orbitals more strongly than the core orbitals, so core orbitals of MOs are much more similar to their atomic counterparts compared to the valence orbitals. In the thesis, we probed both valence and core-levels of molecules.

2.2 Potential Energy Curves

Molecules always have some most suitable geometry with a minimum energy. There is an equilibrium distance between the atoms in this preferred geometry, and energy is required to move apart atoms from each other or closer to each other. Figure 2.3 shows a schematic potential energy curve i.e. energy as a function of intermolecular distance.

To visualize potential energy curves, different approximations have been developed:

(i) *Parabolic Approximation*: This approximation is valid close to the equilibrium distance R_e .

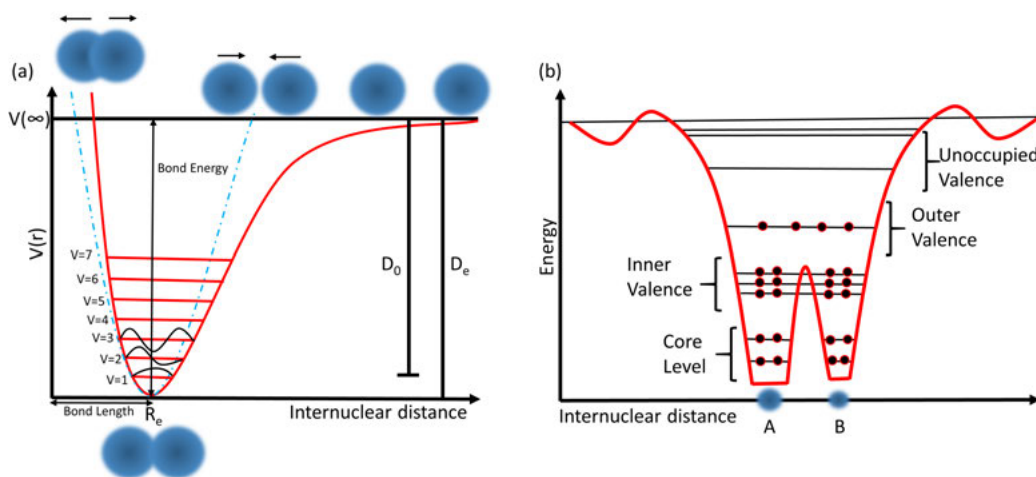


Figure 2.3: (a) A schematic potential energy curve of a diatomic molecule showing a Morse potential (red line) and a parabolic approximation (blue line). (b) A schematic of the diatomic molecule with orbitals energy levels.

(ii) *Morse Potential*: For larger intermolecular distance, a more accurate approximation is needed to model the potential energy curve. Morse potential is mostly used to describe the potential energy for diatomic molecules, and it takes into account the bond breaking of the molecule. The Morse potential has the following potential energy function:

$$V(r) = D_e \cdot (1 - e^{-a(r-R_e)})^2 \quad (2.3)$$

In the equation 2.3, $V(r)$ is the potential energy, D_e is the depth of the well, R_e is the equilibrium distance, r is the intermolecular distance, and a is the width of the potential well (the smaller the number the larger is the width) [26, 27].

The dissociation energy (D_0) is a little different from the depth of the potential well (D_e). D_0 is defined as the minimum energy required to convert the bound state (lowest possible state) of the molecule to a state with an infinite internuclear distance. For a diatomic molecule, the dissociation energy D_0 is of the order of few eV. For covalently bound molecules (e.g., hydrocarbons studied in this thesis), the internuclear equilibrium distances between bound atoms are the order of 1-3 Å [26].

The Morse potential is accurate and useful for a diatomic molecule. For polyatomic molecules, the potential is replaced by a multidimensional potential energy surface. More rotational and vibrational modes exist, and the potential is generally more complex.

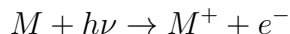
2.3 Light-Matter Interaction

2.3 *Light-Matter Interaction*

Electromagnetic radiation can be described as small discrete energy packets called photons because of the wave-particle duality. Every photon has a discrete energy $E = h\nu$, where h is Planck’s constant and ν the frequency of the light. When photons with energy more than some specific energy interact with electrons occupying the atomic or molecular orbitals, different electronic transitions occur. In these electronic transitions, one quantum state changes to another state, following a defined set of rules. These electronic transitions provide information about the structure of a molecule or an atom and molecule’s dissociation mechanism. Some of these electronic transitions are described below.

2.3.1 *Photoionization or Photoelectric Effect*

One of the most important and commonly occurring electronic transitions due to photon-electron interaction is called the photoelectric effect or photoionization. The photoelectric effect was discovered by Heinrich Hertz in 1887 [28], and explained by Einstein in 1905 [29]. In this process, a photon with energy $h\nu$ greater than the electron’s binding energy interacts with a specific atomic orbital, causing the electron from that orbital to be ejected into the continuum, and photoionization will occur. The schematic diagram is shown in figure 2.4 and the process can be written as:



The electron kicked out from the atom is called a *photoelectron*. The energy of the photoelectron depends on the energy of the photons $h\nu$. The photoelectron energy, according to Einstein equation, is the following:

$$KE = h\nu - BE \tag{2.4}$$

In the equation 2.4, KE is the kinetic energy of the photoelectron, BE is the binding energy required to remove an electron from a specific orbital of the atom/molecule. In molecules, photoionization can be accompanied by vibrational and rotational excitations [30–32]. Koopman’s theorem is a first approximation to the binding energy calculation [33]. According to the theorem, the first ionization energy of the molecule (or atom) is equal to the negative value of the orbital energy. Photoionization can lead to dissociation of the molecule, which is described in section 2.4. The probability for photoionization depends on the *photoionization cross-section*. The cross-section varies from orbital to orbital and element to element as a function of photon energy. The ionization cross-section is most commonly maximum close to the threshold ionization energies and decreases with increasing photon

energy. Different photon energies are required to probe different orbitals. Using ultraviolet (UV) light we can probe outer valence orbitals. Soft X-ray allows probing inner valence and some core-levels, and with hard X-rays the innermost core-levels of high atomic number elements can be reached.

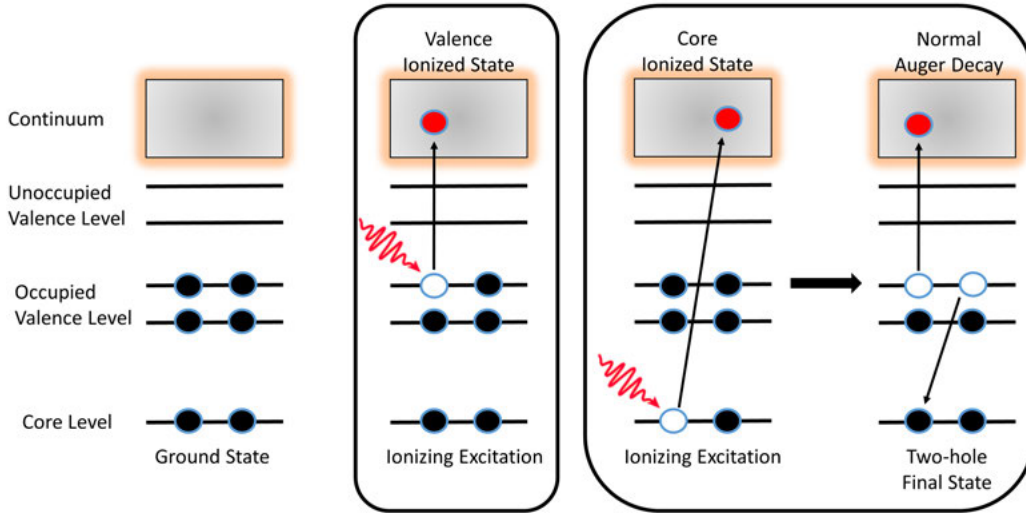


Figure 2.4: Schematic of photoionization of valence- and core-level and core-level relaxation process leading to a normal Auger decay.

Normal Auger Decay

As a core-level of an atom is photoionized, a hole is created in the core orbital. This leaves the atom in a highly excited and unstable form leading to deexcitation via radiative (explained afterwards) or non-radiative processes. When dealing with light elements ($Z < 30$), the non-radiative Auger process is more dominant [24]. In a normal Auger decay, the core hole is filled by an electron from one of the higher orbitals (valence orbitals), and at the same time, another electron, called the *Auger electron*, is emitted, as shown in the figure 2.4. After the Auger decay, the atom is in a doubly ionized state because of the ejection of two electrons (photo and Auger electron) [34]. The normal Auger decay does not follow electric dipole selection rules [25].

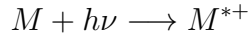
$$M \longrightarrow M^{*+} + e_p \longrightarrow M^{++} + e_A$$

The Auger electron's kinetic energy is defined as the energy difference between the core ionized state (intermediate state) and the doubly charged state (final state).

2.3 Light-Matter Interaction

2.3.2 Photoexcitation or Resonant Excitation

Atoms have occupied and unoccupied orbitals; if the photon energy $h\nu$ is lower than the binding energy, electron from a specific orbital can move from an occupied orbital to an unoccupied orbital. This process is known as a photoexcitation or a resonant excitation and can be written as:



The photoexcitation or resonant excitation is only possible if photon energy matches the following condition:

$$h\nu = E_{excited-state} - E_{ground-state} \quad (2.5)$$

In the equation 2.5, $E_{ground-state}$ and $E_{excited-state}$ are the energies of the ground state and the excited state, respectively[30, 35]. This excited state is unstable and eventually decays into some stable state by fragmentation and/or resonant electron decay. The schematic of the process is shown in figure 2.5.

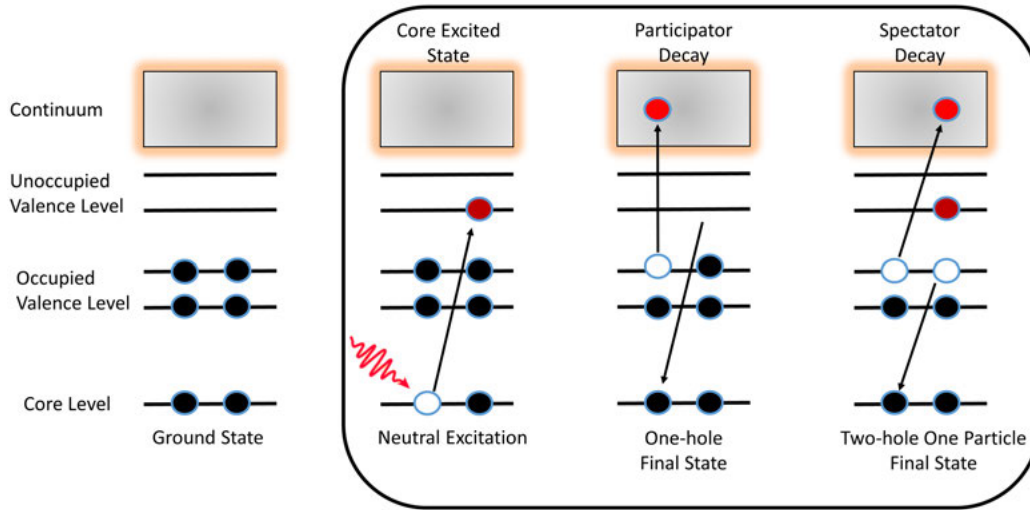


Figure 2.5: Schematic of core-level photoexcitation of the electron and relaxation process showing resonant Auger decay (participator or spectator decay).

Photoexcitation follows the set of rules based on the *electric dipole approximation*. The approximation is applicable for UV and soft X-ray regions; for higher interaction energies, higher multipoles of electromagnetic radiation also contribute. The result of the electric dipole approximation is the electric dipole selection rules. The transition moment integral is the basis of

spectroscopic selection rules:

$$\vec{M} = \int \psi_f^* \mu \psi_i d\tau \quad (2.6)$$

In equation 2.6, \vec{M} is the transition moment, ψ_i is the wavefunction of initial state, ψ_f^* is a conjugate of the wavefunction of final state, μ is the dipole moment operator, and $d\tau$ is the infinitesimal element. For example in molecules, the total spin cannot change, $\Delta S = 0$; for multiplets, the rule $\Delta \Sigma = 0$ hold and the total angular momentum change should be $\Delta \Lambda = 0, \pm 1$ ($\Lambda_i = 0$ to $\Lambda_f = 0$ is forbidden) [36, 37]. The initial and final state have to be of opposite parity. The transition in any quantum mechanical system is governed by these selection rules [26, 38].

Resonant Auger Decay

As one of the atom's core-levels is photoexcited, the atom or molecule will go into an unstable excited state that leads to the deexcitation of the atom and molecule into some more stable state. The core hole is then filled like in the normal Auger decay and singly charged states are produced. This process is called a resonant Auger decay, and the electron ejected is called a *resonant Auger electron*. The ejected electron energy will be equal to the excess energy of the transition[39]. The schematic is shown in figure 2.5 and process is described as:



The resonant Auger decay is further classified into two different categories, based on whether the initially excited electron participates in the relaxation process or not[40, 41].

(i) *Participator Resonant Decay*: In this decay, the excited electron participates in the relaxation process and can go back into the original core-level or be ejected as the resonant Auger electron, as shown in figure 2.5. The participator resonant decay results in valence single-hole states like direct valence ionization.

(ii) *Spectator Resonant Decay*: In this decay, the core-excited electron will act as the observer and does not participate in the relaxation process. The resonant Auger electron will be from another orbital instead of the excited core electron. The spectator resonant decay results in a valence two-hole/one-particle states. Spectator decay final states can also be accessed through the combined ionization and shake-up process.

The normal Auger decay can be easily probed by any ionization source like

2.3 Light-Matter Interaction

ion, electron, or photon bombardment. For probing resonant auger decay, tunable synchrotron is a convenient source, but this can also be achieved by other sources like energetic particle collisions.

2.3.3 *Fluorescence Decay*

As we described earlier, in photoionization and photoexcitation processes when a photon interacts with the matter, an electron may be ejected after the relaxation. However, there is also a decay where a photon is emitted after or during the relaxation. This process is known as a fluorescence decay [42, 43]. The schematic is shown in figure 2.6 and processes are described below.

(i) Fluorescence Decay by Photoionization: $M + h\nu \longrightarrow M^+ + h\nu' + e^-$

(ii) Fluorescence Decay by Photoexcitation: $M + h\nu \longrightarrow M^* + h\nu'$

2.3.4 *Spectroscopy Techniques*

There are experimental techniques used to study atoms and molecules based on the above electronic transitions. *Ultraviolet photoelectron spectroscopy* (UPS) is used to study the atoms' and molecules' valence electronic structure. In UPS, ultraviolet light is used to irradiate the sample, and then the kinetic energy of the emitted electrons is measured with the help of an electron spectrometer. Likewise, *X-ray photoelectron spectroscopy* (XPS) is used to study core-level electrons, and the sample is irradiated with X-rays instead of UV.

Moreover, non-radiative decay processes are studied with *Auger Electron Spectroscopy* (AES) or *Resonant Auger Spectroscopy* (RAS). AES and RAS can help us to study the relaxation processes and to get information about the orbitals taking part in the decay of an excited atom or a molecule. If the atoms or molecules decay by ejecting photons, to study this decay process, if it is non-resonant, then *X-ray Emission Spectroscopy* (XES) is used, and if it is resonant, then *Resonant Inelastic X-ray Scattering* (RIXS) is used. All the above experimental techniques help us to understand the atom's or molecule's electronic structure as a whole.

In this thesis, we apply some of these techniques for a molecular-level understanding of our systems. In **Paper I** and **Paper II**, we collected outer valence electrons using UPS and core electrons using XPS techniques, and photoelectrons acted as start pulse for ion extraction for a time-of-flight (TOF)

spectrometer used in electron-ion coincidence technique. In **Paper III**, we collected core and Auger electrons in total and partial electron yield modes in order to obtain X-ray absorption spectra (XAS).

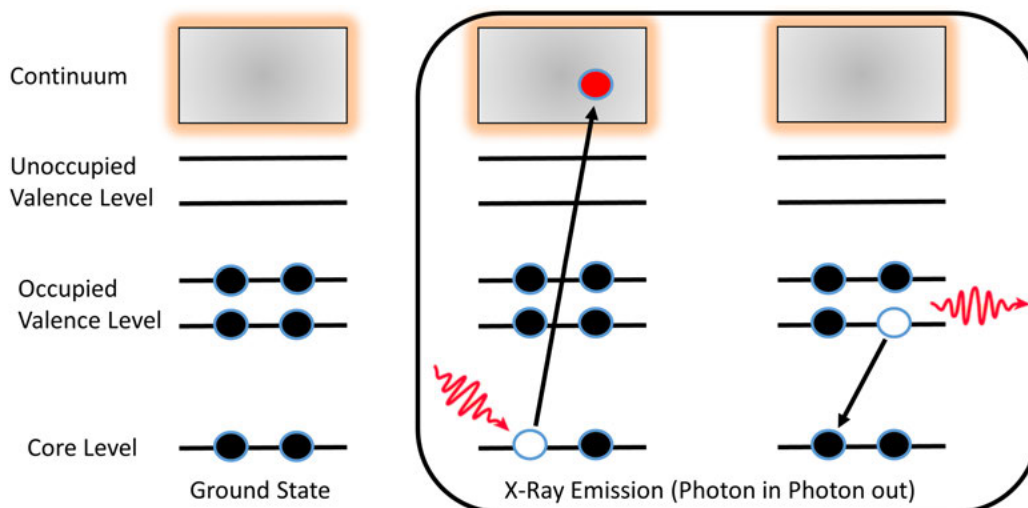


Figure 2.6: A Schematic of the core-level photoionization and relaxation process with the emission of a photon.

2.4 Molecular Dissociation and Fragmentation

When a molecule absorbs energy and increases its internal energy, the molecule rearranges itself or dissociates and fragments into smaller parts to reduce its energy. The electrons can be ejected at any stage (before, during, and after) of the dissociation process. These electrons give qualitative and quantitative information about the dissociation processes [44]. The ions created by these dissociation processes are also studied using different ion detection techniques. In this thesis, positive ions are studied with a TOF spectrometer.

In the well-known *Born-Oppenheimer (BO) approximation*, the electron's movement is considered to be much faster than the nuclear motion due to the difference in the mass of the nucleus and electron. We can thus separate the electronic and nuclear wavefunctions of the molecule, and the BO approximation is based on two underlying assumptions [45]:

- (1) Nuclear motion occurs in a smeared out potential from the fast electrons.
- (2) The electronic wavefunction depends upon nuclear positions but not velocities.

2.4 Molecular Dissociation and Fragmentation

Equations 2.7a & 2.7b are two different ways for mathematical representation of the BO approximation.

$$\psi_{molecule} = \psi_{electron} \cdot \psi_{nuclei} \quad (2.7a)$$

$$E_{total} = E_{electronic} + E_{vibrational} + E_{rotational} + E_{nuclear-spin} \quad (2.7b)$$

Equation 2.7a describes the wavefunction of the molecule as product of electronic ($\psi_{electron}$) and nuclear (ψ_{nuclei}) wavefunctions. In equation 2.7b, the molecular energy is the sum of all independent terms with different order of magnitude.

An electronic transition happens fast from one state to another without any change in the molecule's nuclear geometry and thus vertically between potential energy curves, defining the so called *Franck-condon region*, indicated as grey arrows in figure 2.7.

Within the Frank-Condon region, the ground state of the molecule can reach two different excited states [26]:

- (1) Represents the dissociative states of the molecule with the absence of the vibrational feature of the molecule. Observed with photoelectron spectroscopy, such a state results in unresolved bands with no vibrational band features.
- (2) This excited state leads to the dissociation of the molecules if and only if the electronic transition happens above dissociation limit of the state.

Other dissociation mechanisms go beyond the BO approximation, for example *predissociation*. In this, the molecule first is excited to a higher vibrational state of a bound state [32, 46]. After that, the rearrangement of the electronic energy leads to a non-radiative transition from the bound to an unbound state. In a polyatomic molecule, predissociation is more probable than direct dissociation as several vibrational modes and many crossing potential energy surfaces are present. In this dissociation pattern, the vibrational energy is transferred or rearranged between vibrational modes leading to the dissociation of the molecule [44].

After valence ionization, the molecule, which is in a single hole (singly charged) state, may be bound (with a possible change in internuclear distance) or dis-

sociative. Fragmentation depends on the molecular orbital nature; if the ionization happened from the non-bonding *highest occupied molecular orbital* (HOMO), then it is not followed by any fragmentation and remains in a bound state. Ionization from other valence orbitals almost always leads to fragmentation [47, 48].

Core-level photoexcitation or photoionization excites the system to highly excited states, the relaxation of which may lead to different fragmentation patterns. After the Auger decay, the ionized state created is often unstable and prone to the fragmentation of the molecule, especially the doubly ionized state created by normal Auger decay [44, 49]. Resonant Auger relaxation with a subsequent dissociation is shown in figure 2.7(b). All the dissociation mechanisms obey the law of conservation of energy and momentum and if we study different relations like photofragments' velocity and angular momenta [50–52], then we can find out more about photodissociation and fragmentation reactions.

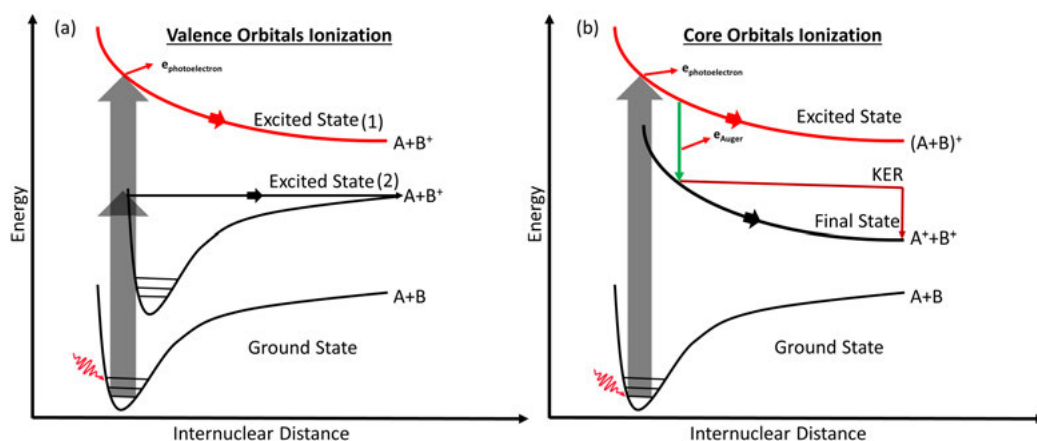


Figure 2.7: (a) Schematic of valence dissociation of the molecule. (b) Schematic of core dissociation of the molecule.

After charge separation of doubly ionized molecule, the total kinetic energy of the fragments (called *Kinetic Energy Release* (KER)) depends on the nature of the repulsive final state. The KER is distributed or shared by fragments, depends on the relative masses due to conservation of momentum. The KER contains much information on the dissociation dynamics and energetics [53]. The KER is depicted on the potential energy curve, as shown in figure 2.7 after Auger relaxation. Sometimes direct fragmentation can also lead to the KER [39].

Ionization with subsequent decay occur on a timescale of a few femtoseconds.

2.4 Molecular Dissociation and Fragmentation

Electronic decay and nuclear motion are two different competing processes during the relaxation of the core-excited state. These competing processes have different effects on Auger electron spectrum. If the dissociation takes place before electronic decay the process, it is called *ultrafast dissociation* (UFD). If a core-electron is promoted to an antibonding orbital, a fast nuclear separation may follow, and the initial core hole is left with one of the fragments. The core hole decay proceeds in a different chemical environment with different energy levels, for example in a single atom instead of a molecule [54, 55]. In the Auger electron spectrum this is seen as sharp atomic-like features overlapping broad molecular Auger spectrum from transitions which took place before the molecule had time to fragment.

This thesis (**Papers I & II**) explores both valence- and core-level regimes as described above for molecular dissociation and fragmentation. To study the dissociation dynamics of the molecules, we used *photoelectron photoion coincidence* (PEPICO) methods, with detection of one or several ions in coincidence with photoelectrons originating from the same ionization event. [56, 57].

Synchrotron Radiation and Sample Delivery Systems

3.1 *Synchrotron Radiation*

Electromagnetic radiation is created if the velocity of a moving charged particle changes [58]. If the charged particle moves along a circular path with *relativistic velocity*, it emits radiation known as synchrotron radiation. In 1946, synchrotron radiation was first observed at a General Electric accelerator [59]. First, the synchrotron radiation was considered to be detrimental for particle accelerator operation, but with time it was realized that synchrotron radiation could be beneficial for numerous scientific research applications [60]. Nowadays, synchrotron radiation is widely used in different fields, such as physics, chemistry, material science, engineering, and life sciences. There are numerous descriptions of synchrotron radiation and its applications in the literature [60–63].

At synchrotron radiation facilities worldwide, the radiation is produced when trajectories of relativistic electrons are deflected by different magnetic structures. The schematic shown in figure 3.1 highlights the basics of the generation of synchrotron radiation. High-velocity electrons are produced by an electron gun - a linac, or a similar device¹ then injects high-velocity electrons into a storage ring. A *radio-frequency (RF) cavity* feeds energy to stored electrons to compensate for energy losses by radiation emission and helps electrons to maintain a fixed orbit around the storage ring. Other than bending magnets, the storage ring also contains some quadrupole and hexapole magnets to keep the electron beam focused.

Insertion devices are significant part of modern synchrotron storage rings. Plus providing more flexible polarization is to provide more intense radiation

¹Like SOLEIL in France, after electrons are generated, enter into a booster ring, where electrons are accelerated more until they get nominal energy, and then they are injected into the storage ring.

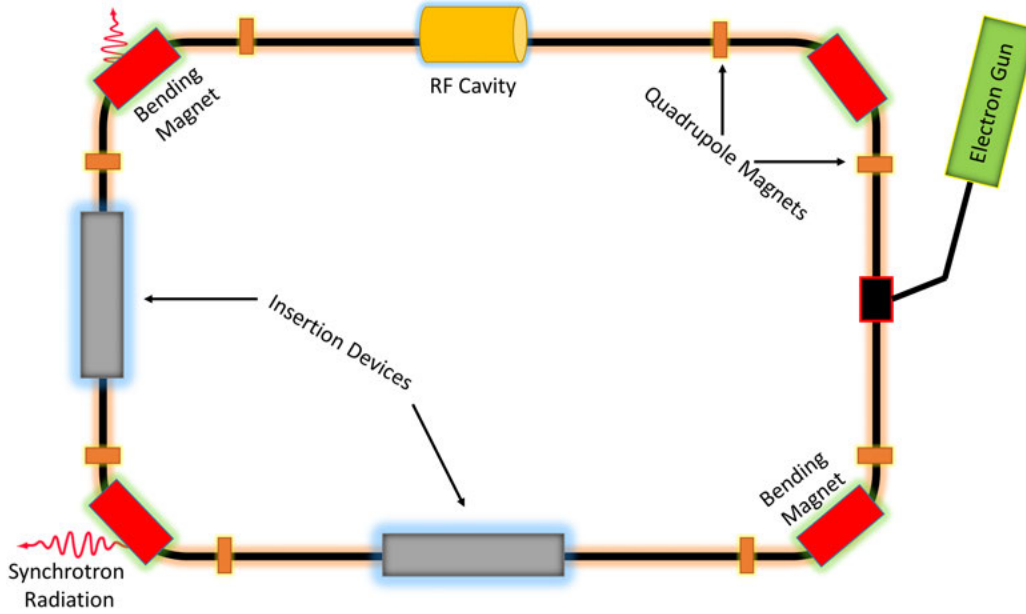


Figure 3.1: Schematics of a synchrotron radiation source.

compared to using bending magnets only. A usual insertion device comprises arrays of magnets, which force relativistic electrons to oscillate instead of moving in a straight trajectory. Due to the acceleration associated with these oscillations, synchrotron radiation is produced in the insertion device. Insertion devices can be of different types, such as *undulators* or *wigglers*. In this thesis, all of the beamlines we have done our experiments are based on undulators.

Figure 3.2 shows an overview of the MAX IV Laboratory, Lund, Sweden. The MAX IV facility consists of a linear accelerator (Linac) and two electron storage rings for the generation of synchrotron radiation. The MAX IV facility Linac is roughly 300 m long and accelerates electrons to 3 GeV energy. When the Linac is not injecting electrons to storage rings, it can provide electron bunches to the short-pulse-facility (SPF). Two storage rings are used to generate synchrotron radiation for a wide energy range from microwave to hard X-ray. The big 3 GeV storage ring has a circumference of 528 m and a maximum design current of 500 mA. This storage ring is optimized for the generation of high brightness hard x-rays. The small 1.5 GeV storage ring has a circumference of 96 m and a maximum design current of 500 mA. This storage ring is designed for the generation of radiation from microwaves to soft X-rays [64]. In my thesis, all the experiments were done at small storage ring.

3.2 Characteristics of Synchrotron Radiation

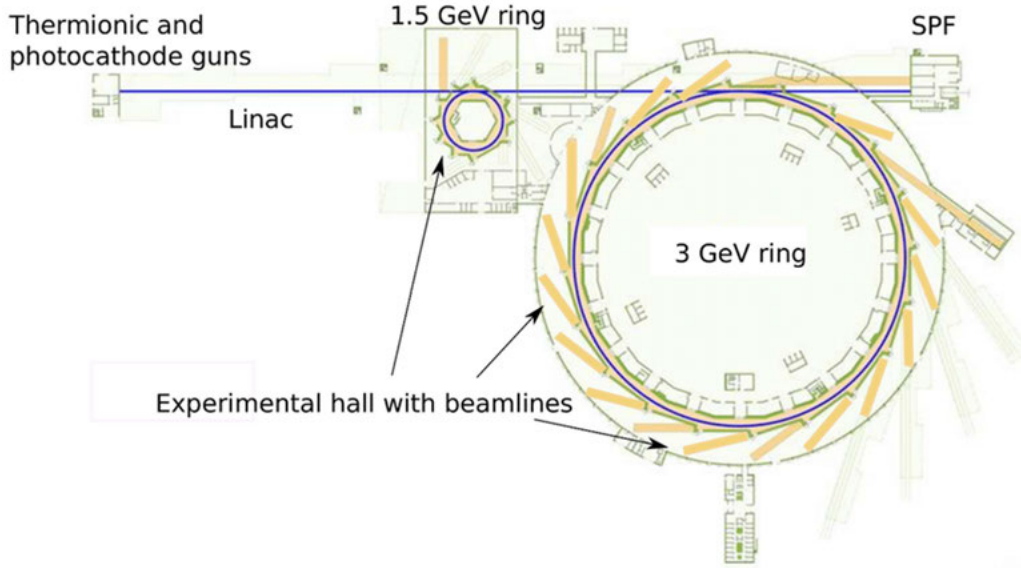


Figure 3.2: The layout diagram of the MAX IV synchrotron radiation facility. (Drawing by Johnny Kvistholm from MAX IV Laboratory, Sweden)

3.2 Characteristics of Synchrotron Radiation

Compared to traditional X-ray gas discharge lamps or tubes, synchrotron radiation has superior properties for characterization and probing different materials and processes at the atomic and molecular levels. Synchrotron radiation delivers a continuous energy spectrum and higher brightness. A specific photon energy can be chosen from an undulator-generated photon beam with the help of a monochromator in a wide energy range from microwaves to hard X-rays. High source stability, high brilliance, and variable polarization (both linear and circular) are also different merits of synchrotron radiation, distinguishing it from traditional sources [65]. These characteristics are linked to the relativistic velocity of the charged particles emitting radiation [66]. In this thesis, we used different characteristics of synchrotron radiation like tunability, high photon flux and high stability to study our samples from different perspectives.

3.2.1 Undulator Radiation

An undulator is a type of an insertion device consisting of two arrays of magnets with alternating pole separated by a gap, as shown in figure 3.3. When an electron comes into the undulator, the electron starts oscillating in the plane perpendicular to the magnetic field. The distance between two magnets of the same polarity is known as the *oscillation period* or *undulator spatial period* (λ_u).

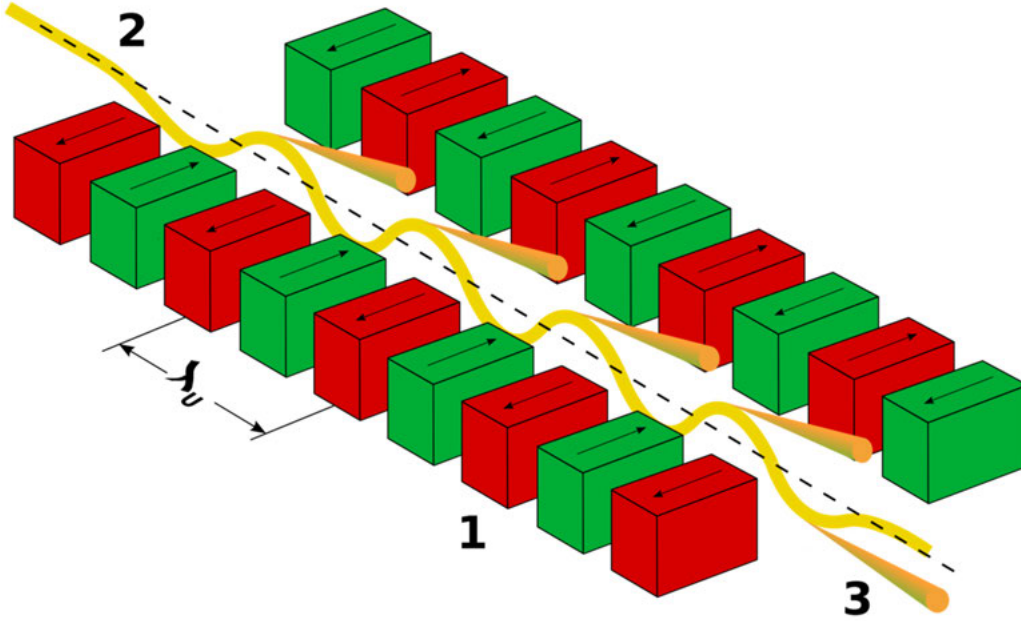


Figure 3.3: Working principle of the undulator. (1) magnets, (2) electron beam entering from the upper left, (3) synchrotron radiation exiting to the lower right[67]

The *undulator strength parameter* is estimated as follows:

$$K = \frac{eB\lambda_u}{2\pi m_e c} \quad (3.1)$$

Where e is electron charge, B is the magnetic field strength, λ_u is the oscillation period, m_e is the mass of the electron, and c is the speed of light. For $K \ll 1$, the small oscillation amplitude will give narrow energy bands due to constructive interference of radiation emitted at different oscillations (undulator), and $K \gg 1$ will give a broad energy band due to the radiation contribution of each period summing up (wiggler) [68].

The emitted photon energy can in principle be controlled by varying the magnets strength, but in practice, the undulator gap is the most easily changeable parameter. By changing the magnetic arrays of the undulator, we can also change the light polarization. An example of a FinEstBeAMS beamline undulator spectrum is shown in figure 3.4. The undulator peaks are not evenly spaced because monochromator's contribution of diffraction orders.

3.3 FinEstBeAMS Beamline at MAX IV

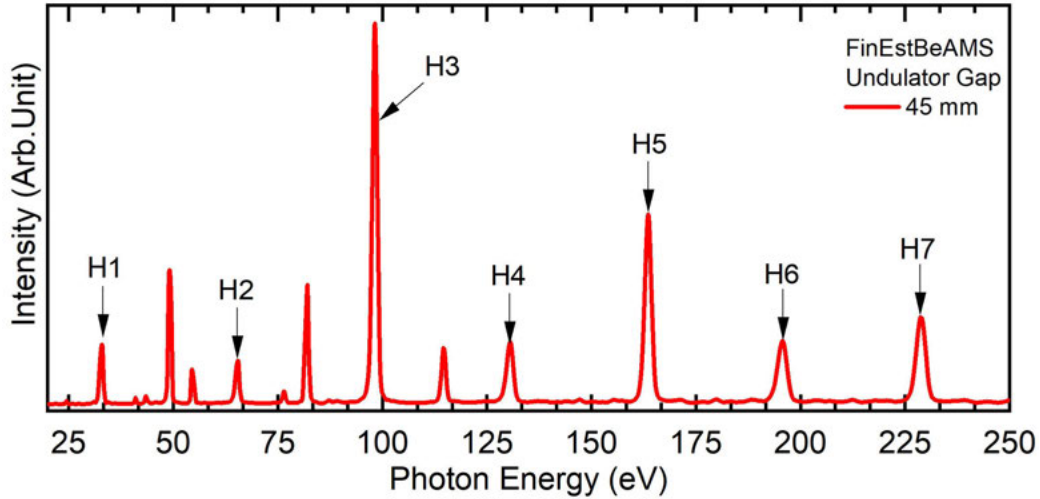


Figure 3.4: An example of a FinEstBeAMS beamline’s undulator energy spectrum, measured at 45 mm gap.

3.3 *FinEstBeAMS Beamline at MAX IV*

Most of the experiments in this thesis were done at FinEstBeAMS² beamline [69, 70] located at 1.5 GeV storage ring of MAX IV. The beamline has been designed to produce a wide energy range of radiation from 4.3 eV (ultraviolet) to 1000 eV (soft X-rays). The specially designed *elliptically polarizing undulator* (EPU) is used together with a *plane grating monochromator* (PGM). The EPU is a straight region of 2.5 m length with 25 full periods of 95.2 mm and half a period at each end. The plane grating monochromator is illuminated with collimated light (cPGM). To change energy during experiment, both undulator and monochromator is used, monochromator selects the energy from a broad undulator energy peak. Four different mirrors from the undulator to endstation are used to focus and defocus the light at endstation. The water-cooled *toroidal mirror* (M1) and the *plane mirror* (M2) take the beam from the undulator, and most of the heat is absorbed here. The M1 and M2 mirrors collimate the beam both vertically and horizontally. The cPGM has two types of gratings, one for low photon energies (92 l/mm) and one for high photon energies (600 l/mm). The uncooled *toroidal mirror* (M3) is used to refocus the beam, which is dispersed after monochromator. The smallest spot size of the beamline is approximately. 100 $\mu\text{m} \times 100 \mu\text{m}$, which is achieved by using the *ellipsoidal refocusing mirror* (M4). The detailed optics layout of the beamline is shown in figure 3.5. The total power accepted by the beamline is about 600 W. The estimated photon flux at the sample is estimated from 8×10^{13} photons/s to 8×10^{11} photons/s (between

²Finnish-Estonian Beamline for Atmospheric and Material Science

4.3 to 800 eV) and 10^{12} photons/s (>1000 eV). At the low photon energy, there is some higher-order light from the undulator that can be suppressed using different kinds of filters like LiF filter for energy up to 11.8 eV and Mg filters energies from 25 to 50 eV with the low energy grating.

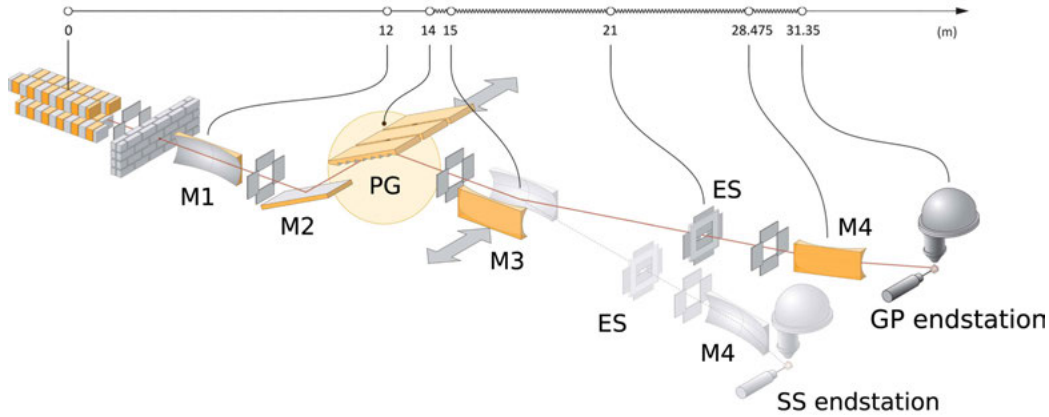


Figure 3.5: The optical layout of the FinEstBeAMS beamline at MAX IV. M1-M4= Mirrors, PG=Plane Grating, ES=Exit Slit, SS=Solid State, and GP=Gas-Phase. (From Pärna R *et al.* (2017), *Nucl. Instrum. Methods Phys. Res. A*, **859**, pp.85. Reproduced with permission © 2017 Elsevier B.V.)

FinEstBeAMS beamline has two branches, dedicated to gas-phase and solid-state studies. In this thesis, we have done all of our experiments at the gas-phase endstation. The gas-phase endstation provides sample environments for different types of samples from single-molecule vapors to clusters. The gas-phase experiments are not appropriate for the UHV conditions necessary in the beamline, therefore the endstation also has a differential pumping section. The differential pumping section consists of three stages; a 300 l/s turbomolecular pump, a line-of-sight differential ion pump, and a 75-80 l/s ion pump. The differential pumping section helps to maintain vacuum and also protect the optics of the beamline. The gas-phase endstation has two chambers; an upstream chamber and a downstream chamber. The downstream chamber is equipped for photo-luminescence experiments. However, we did all experiments in this thesis at the upstream chamber, consisting of a Scienta R4000 electron spectrometer, equipped with a *fast position-sensitive detector* for photo-electron, photo-ion (photo-ion) coincidence measurements (PEPI(PI)CO). The electron spectrometer can also be used separately for high-resolution electron spectroscopy of gas-phase samples. The time-of-flight (TOF) spectrometer capable of *multi hit momentum imaging* is also part of the upstream chamber. As per requirement, the ion spectrometer is removable and can be stored at a separate storage chamber. The endstation

3.4 Sample Delivery Systems

interaction chamber is rotatable around the beam axis of the beamline from the Scienta spectrometer’s horizontal to vertical position under vacuum. This rotation is beneficial in combination with selecting the polarization plane of the helical undulator. The rotation is also beneficial for access to a larger port easily for mounting some specialized equipment, for example we inserted a resistive oven from that larger port to introduce the sample inside the chamber³. A custom made software is developed to communicate between the TOF spectrometer and electron spectrometer for PEPI(PI)CO studies in gas-phase. The ion and electron coincidence acquisition is performed using the *CoboldPC software*. In **Papers I & II** all experiments are done at the FinEstBEAMS beamline. Figure 3.6 shows a drawing of the GPES and red arrows indicates the important components of endstation.

Moreover, in **Paper III** of this thesis, we used similar beamlines for different experiments. We used the PLEIADES⁴ beamline at SOLEIL synchrotron radiation facility, Paris, France, to study nanoparticles by XAS in TEY mode. We also used the FlexPES⁵ beamline at MAX IV synchrotron facility, Lund, Sweden, for liquid-jet XAS studies in PEY mode.

3.4 Sample Delivery Systems

3.4.1 Vapor Production

At room temperature and pressure, many organic compounds are solid. Electron and ion spectroscopy of free molecules of such organic samples need some method to produce isolated molecular vapor. One of the easiest ways to produce vapor is to heat the material as the vapor pressure of material increases with temperature. For the low-temperature vapor production of the organic sample, a *resistive oven* has been used. Our research group designed this resistive oven at the University of Oulu. The schematics of the oven is shown in figure 3.7.

In this oven, a resistively heated wire is encircled around a crucible. The crucible is heated by thermal conduction and radiation. During the heating, most of the heat losses are by radiation. To minimize heat losses, special heat shields can be used. There is the option to use water cooling for extra cooling, but in this thesis, we did not use that because our temperature is not that high during the experimentation. In the experiments of **Papers I & II**, stainless steel crucibles were used. We monitored the TOF mass spectra as function of temperature to detect any thermal sample deterioration, and

³Figure 3.6a shows the overall drawing of endstation in chapter 4

⁴Polarized Light source for Electron and Ion Analysis from Diluted Excited Species

⁵Flexible Photo Electron Spectroscopy

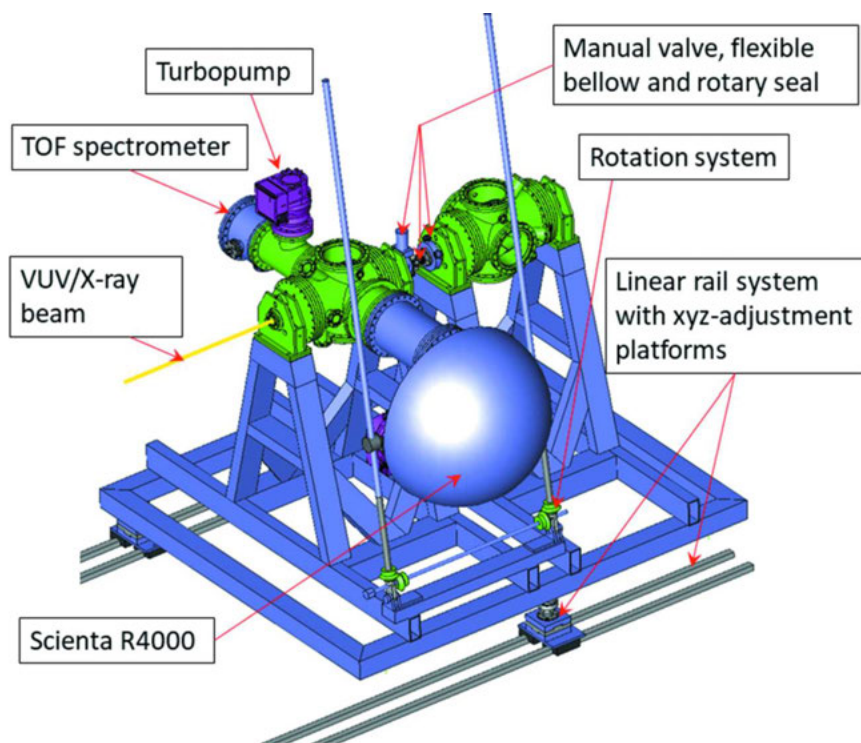


Figure 3.6: The main component of Gas-Phase End Station(GPES) at FinEstBeAms Beamline at MAX IV, Synchrotron facility, Sweden. Main components labelled with red arrows. (From Kooser K. *et al.* (2020), *J. Synchrotron Radiat.*, **27**, pp.1082. Reproduced under CC-BY 3.0)

established a suitable working temperature before the actual measurement.

3.4.2 Free-Standing Nanoparticles Preparation

In **Paper III**, free nanoparticles were prepared from hydrated conditions (from solution form) by a *constant output atomizer* (N° 3076, TSI Inc) [71]. Then these generated hydrated nanoparticles are dried by *diffusion-based silica driers* (model 3062, TSI Inc) [72] at different relative humidity (RH) levels ranging from 11% to 85%. Afterwards, these dried nanoparticles were passed through an *aerodynamic lens* (ALS) to the interaction chamber, as shown in figure 3.8.

The constant output atomizer is used to atomize different solutions and suspensions. The compressed gas, also known as the carrier gas, is expanded through an orifice to form a high-velocity jet. Through the vertical passage, the solution is brought near the atomizing section, then atomized by the jet, and coarse particles are impacted on the wall opposite to the jet. This way, the impacted particles drain back to the solution container at the atomizer

3.4 Sample Delivery Systems

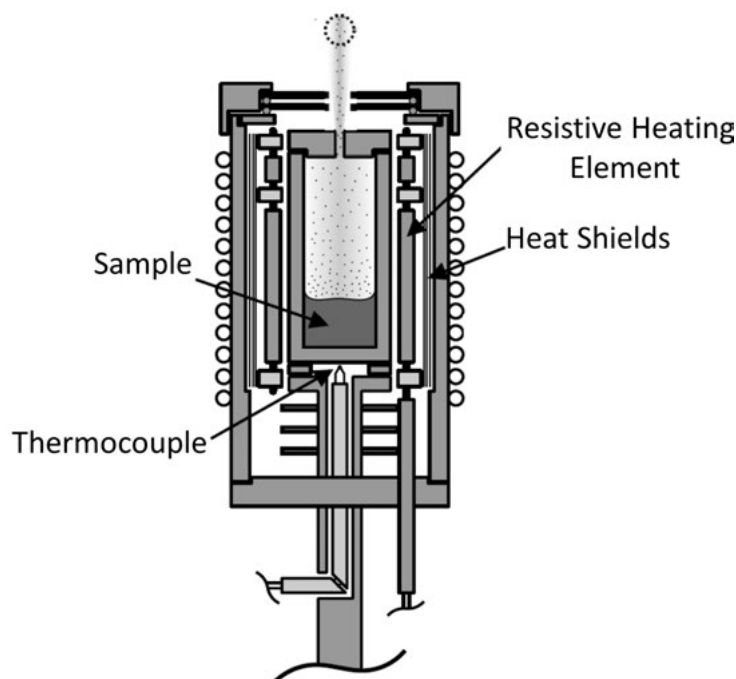


Figure 3.7: Schematic layout of the resistive wire oven.

assembly block. Small particles move in the opposite direction out of the atomizer.

Two diffusion dryers were used to dry hydrated salt nanoparticles. These diffusion dryers are designed as a general-purpose diffusion dryer to dry wet-particles with a slight loss of particles. The inlet of the diffusion dryer is integrated to a water trap system to catch the coarse particles. The dryer consists of two concentric cylinders; the drying agent, silica gel, is placed between the acrylic outer cylinder and wired screen cylinder. As the hydrated particles pass through the inner cylinder, the water diffuses through the wired cylinder to silica gel. The particle has no direct contact with the silica gel; therefore, the particle loss is minimum. The silica gel can be reused after drying in an oven.

After the nanoparticles are dried by the diffusion dryer, the nanoparticle beam enters the ALS. As we generated salt nanoparticles at atmospheric pressure, the ALS allows us to transfer these nanoparticles from atmospheric pressure into the vacuum chamber. The sequential compression and expansion of carrier gas through a series of coaxial orifices with different diameters help focus the beam of nanoparticles into the interaction chamber. The nanoparticles will separate from the gaseous streamlines after passing through the orifices in the ALS and get focused along the lens symmetry

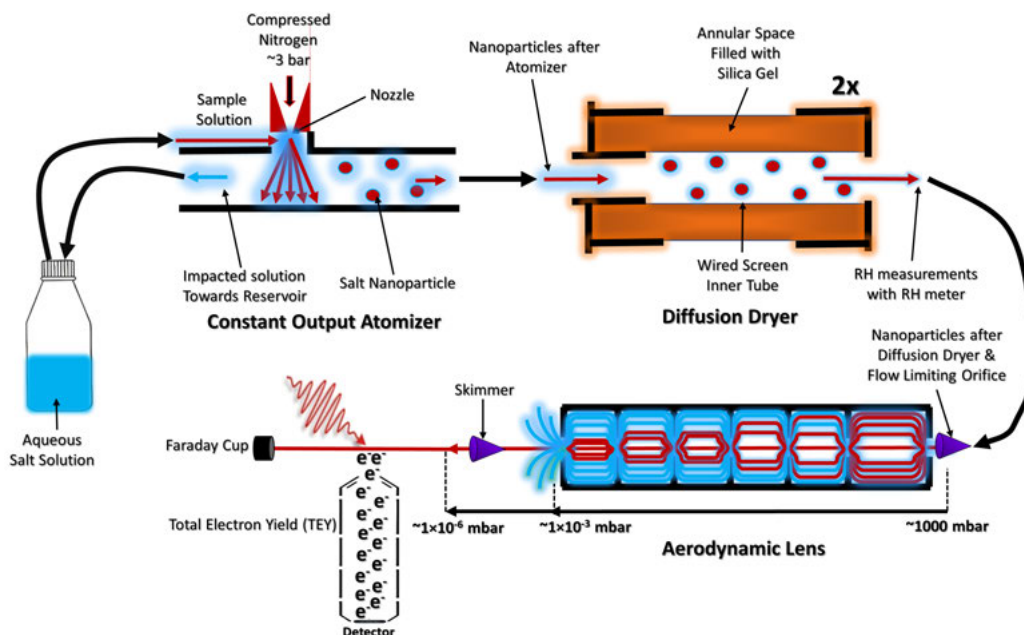


Figure 3.8: Schematic diagram to illustrate generation of free-standing nanoparticles beam. (From Abid A. R. *et al.* (2021), *RSC Adv*, **11**, pp.2104. Reproduced under permission CC-BY 3.0.)

axis by the inertia effect. Figure 3.8 shows the overall representation of nanoparticles generation with the atomizer, drying, and transferring into the interaction chamber.

Using this system we can get particles of a broad size distribution (average diameter of 100-200 nm range) from hydrated condition into a sub-millimeter sized beam inside the interaction chamber.

3.4.3 Liquid-Jet

A liquid-jet setup is used to study different volatile liquids. The liquid-jet was first employed by Faubel *et al.*[73] in 1988. The liquid-jet is produced when a sample solution is pushed with a constant flow rate ($\sim 0.5\text{--}1\text{ ml/min}$) through a converging quartz glass capillary, known as a liquid-jet nozzle. The nozzle opening size is typically $\sim 20\text{--}25\text{ }\mu\text{m}$, determining the size of the jet produced at the rip-off-point⁶. PEEK tubing and filters⁷ are mostly used during experiments. There are three different regions of the liquid-jet:

- (1) After rip-off, the jet has a laminar flow (for $\sim 5\text{--}10\text{ mm}$).

⁶The point where the nozzle opens in the vacuum chamber.

⁷To avoid substantial insoluble contamination and prevent blockages.

3.4 Sample Delivery Systems

- (2) Then it changes into a turbulent flow.
- (3) Eventually, the flow disintegrates into diffuse droplets.

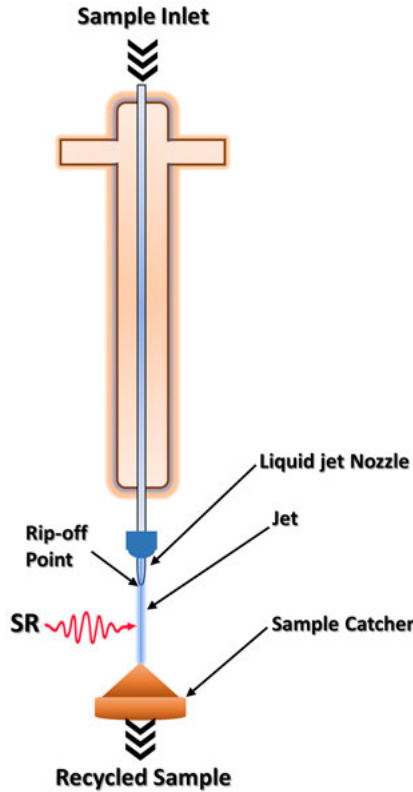


Figure 3.9: Schematic to illustrate liquid-jet setup at VERITAS beamline, MAX IV Laboratory, Sweden. (SR=Synchrotron Radiation)

The jet temperature decreases by evaporative cooling after entering into the vacuum of the experimental chamber [74]. The jet cooling rate is not very well known because of the cut-off in the maximum radial ablation rate. Therefore, it is difficult to predict the temperature of the jet surface. In **Paper III**, the liquid-jet used has no sample disposal, but the sample is caught in the liquid nitrogen trap and cannot be recycled. During my doctoral research secondment at VERITAS beamline, MAX IV Laboratory, Sweden, I participated in the commissioning of the liquid-jet setup, which has a unique sample catcher for recycling samples and a degasser (DEGASi PLUS Semi-Prep 4-ch 925 μ l). Figure 3.9 illustrate the simple schematic of liquid-jet setup at VERITAS beamline. The liquid-jet setup at the FlexPES beamline used in **Paper III** is quite similar to the VERITAS beamline, excluding the catcher system.

Spectroscopic Methods and Data Handling

In this thesis, photoelectron spectroscopy (PES), ion time-of-flight mass spectroscopy (ion TOF-MS), and photoelectron, photoion, (photoion) coincidence spectroscopy (PEPI(PI)CO) were used to study the photofragmentation of the biologically relevant molecules in the gas-phase (**Paper I & II**). X-ray absorption spectroscopy (XAS) was used to learn about changes in the local environment of ions in differently hydrated nanoparticles (**Paper III**). All the experiments were performed with synchrotron radiation, at MAX IV and SOLEIL. Extreme ultraviolet (XUV) or soft X-ray radiation was used to ionize the samples.

4.1 *Electron Spectroscopy*

Electron spectroscopy is based on the photoelectric effect observed by Heinrich Hertz (1887), and later on, this effect was utilized in photoelectron spectroscopy, pioneered by Kai Siegbahn and co-workers [75] in X-ray regime, and David Turner and coworkers in ultraviolet regime [76]. PES has gained much importance in the characterization of different types of matter. After interaction with photons, an ionized molecule or an atom emits electrons carrying plenty of information about the molecular electronic structure. The binding energy is very sensitive to the *chemical environment* of the molecule. The chemical environment is related to the identity, number, and distance of these adjacent neighbors atoms. The intrinsic factor related to the chemical environment is the charge state. The change in the binding energies caused by changes in chemical environment is called *chemical shift* [77]. This property is used in chemical analysis by core-level photoelectron spectroscopy. Valence orbitals participate in bond formation; therefore, chemical shifts are challenging to interpret [32, 77].

Auger spectrum provides information about the multi-ionized molecule's final states, and the core-level photoelectron spectrum can reveal much in-

formation about the molecular structure, for example number and relative abundance of different functional groups. In all cases, the analysis starts by measuring the kinetic energy of the electrons. The most used electron spectrometers today has a *hemispherical deflection electron analyzer* (HDA) as an electron energy analyzer. The simple cut-through diagram¹ of an HDA is shown in figure 3.5. In this thesis, all the electron spectra were measured with the help of an HDA.

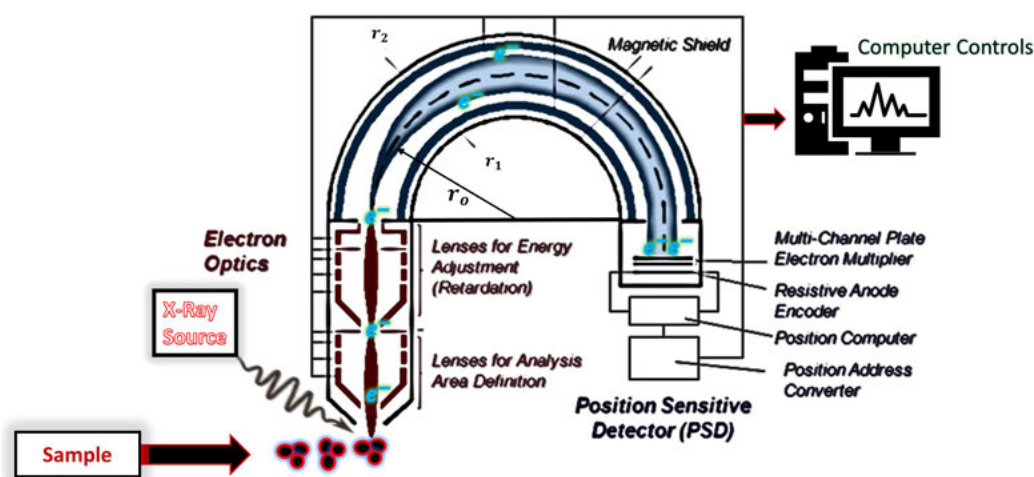


Figure 4.1: Simple cut-through diagram of a hemispherical electron energy analyzer (HDA).

There is a lens system at the HDA entrance to collect and guide the emitted electron towards the entrance slit of the hemisphere. The electrons can be accelerated or decelerated by changing the electric potential of the lenses. The primary function of the lens system is to increase the transmission².

The central part of an HDA consists of two concentric hemispheres acting as electrodes at different potential. The electrons follow a curved path due to the electrostatic force. The average or nominal radius (r_o) of the spheres determines the resolution of the analyzer and the kinetic energy dispersion window of the electrons, in combination with the pass energy and the slit width. The applied electric field between the two electrodes of the analyzer will determine the path of the electron with specific kinetic energy (E_o) along the nominal radius (r_o). Slightly different energies around E_o follow different paths through the analyser, and hit the detector at different positions. The HDA focuses electrons of the same energy entering from different angles to

¹Concept adopted from technical presentation from Vohs J. *et al.*, University of Pennsylvania, USA (2006).

²The ratio between the detected electrons vs emitted electrons is called transmission.

4.1 Electron Spectroscopy

the same x-coordinate of the detector. The transmission of an HDA is defined by the solid angle of acceptance of an analyzer; larger acceptance angle means an increased transmission.

To calculate the constant relative resolution of HDA, following approximate formula can be used:

$$\frac{\Delta E}{E} = \frac{s_1 + s_2}{2r_o} \quad (4.1)$$

In the equation 4.1, s_1 and s_2 are the entrance and exit slit widths, respectively, and r_o is the nominal radius of the analyzer, as shown in figure 4.1. For the position-sensitive analyzer, the width of the exit slit can be substituted with the accuracy of the detector. In addition to that, position-sensitive analyzers improve the intensity because electrons can be collected from a larger area.

The HDA can also be operated with constant absolute resolution (ΔE_a), which is more practical for photoelectron spectroscopy. To achieve a good absolute resolution, high kinetic energy electrons are challenging, and therefore the electrons are retarded before entering in the HDA analyzer to overcome the problem. The pass energy is the actual energy of the electrons after the retardation.

The simple formula for calculating the constant absolute resolution is the following:

$$\Delta E_a = E_{pass} \cdot \frac{s_1}{2r_o} \quad (4.2)$$

We can adjust the resolution and transmission by changing the pass energy and/or width of the entrance slit according to the experiment's requirement. For the measurement, resolution and transmission are critical. These two parameters contradict each other, like increasing resolution (by decreasing width of entrance slit and pass energy), resulting in the decrease in the transmission of electrons and vice versa [78].

When using the electron spectrometer in the coincidence mode, the communication between the electron and TOF spectrometers should be fast, which is achieved by using *micro channel plates* (MCPs) and a resistive anode [79]. The electron output signal has a much shorter delay than the actual electron arrival time with the *resistive anode detector* (RAD). The resistive anode is placed on behind the MCPs, which enhance the electron signal by multiplying each electron hit due to an avalanche effect, as in figure 4.2. When the high energy primary electron hits the micrometer-sized holes of the MCP coated with a material with a low work function, secondary electrons are created, and the electron avalanche reaches then the anode. The signal propagates

to each corner of the anode. By measuring the signal's attenuation from each corner, the hit's position can be measured. The HDA at FinEstBeAMS beamline has three MCPs in a Z-stack configuration and a resistive anode [70].

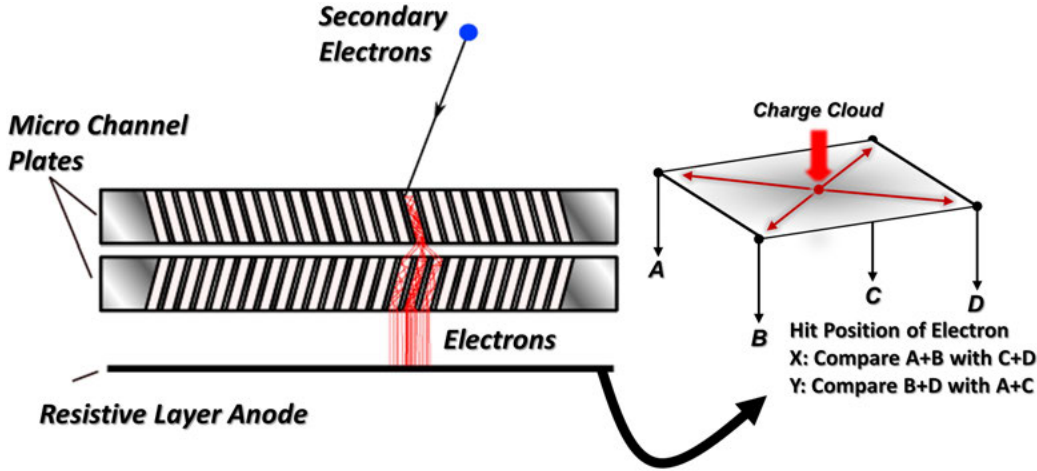


Figure 4.2: Schematic diagram for the detection of an electron at the MCP detector and a resistive anode. (From Rogers A. M *et al.* (2015), *Nucl. Instrum. Methods. Phys. Res. B*, **795**, pp.327. Reproduced with permission © 2015 Elsevier B.V.)

During the coincidence measurements, we used fixed voltages on the HDA. Therefore only electrons from a fixed kinetic energy range were collected. In our HDA type of spectrometer, the kinetic energy window size is roughly 10% of selected pass energy, but depends on the size of the detector in relation to the dispersion of the analyzer. In our measurements, we selected 100 eV pass energy, resulting in an electron kinetic energy window is approx. 10 eV. In the coincidence setting, the HDA is not able to measure the electron energy directly. The software gets only the hit position of the electron in the direction of the electron energy dispersion. The measurement software does not know the connection between the hit position and the energy; therefore, it was done after the measurement with some absolute standard, carbon dioxide (CO_2) in our case. The photoline is moved across the detector by changing the incident photon energy, and then the known kinetic energy vs. detector position is fitted to a second-order polynomial of measured points.

4.2 Time-of-Flight Mass Spectroscopy

In ion time-of-flight mass spectroscopy (ion TOF MS), ions with different mass-to-charge ratios (m/q) are separated based on the flight times between some start pulse (triggered for example by electron detection) and the arrival

4.2 Time-of-Flight Mass Spectroscopy

time to a detector. When ions with the same charge (q) are accelerated to the same kinetic energy, the resulting different velocities of the ions reflect the m/q ratios. Consequently, a heavier ion will move to the detector more slowly than a lighter ion. The mathematical relationship between the TOF and m/q ratio is expressed as the following equation:

$$T = T_0 + C\sqrt{\frac{m}{q}} \quad (4.3)$$

Where T_0 and C are calibration constants that depend on the measurement and spectrometer settings. Several methods exist for the calibration from time-of-flight to m/q scale of the mass spectrum, but we used the most simple and most accurate by using well-known mass peaks. Even at the UHV, there is always residual gases present like H_2O , N_2 , O_2 , and the parent ion for the bigger molecule can also be used as one calibration point.

In a simple form of the ion TOF MS, the ions are first accelerated by an electric field, and after the acceleration region, they are free to move in the field-free drift region towards the detector. This type of mass spectrometer was first developed in 1948[80], and the first scientific investigations were done in 1950. Later on, this spectrometer was further developed and modified by Wiley and McLaren in 1955[81], they suggested a two-stage acceleration of ions (shown in figure 4.3), which improved the mass resolution. In the first stage of acceleration, also called the extraction region, the extraction voltage (V_e) is applied over the sample region. The main purpose of extraction voltage is to guide the ions towards the main acceleration region. In the second stage of acceleration, the acceleration voltage (V_a) is applied to the ions. This accelerates the ions, and the ions enter into the field-free region called drift tube. To compensate for spatial distribution, two-stage ion acceleration of the ions is beneficial.

The ions formed towards a pusher-plate get higher velocities than the ions produced near the acceleration region. Therefore, ions formed towards the pusher plates have slightly longer TOF than ions produced near the acceleration region. Hence ions of the same mass give broader peaks and decrease the spectrum's mass resolution. To make the same mass and charge to come at the detector at the same time, combinations of the applied voltages V_e and V_a are used with a certain ratio to fulfill so-called called *Wiley-McLaren condition* presented in equation 4.4 [82]. If this condition is fulfilled, then the flight time does not depend on the initial position of ion creation and the system is called *space focused*.

$$D_0 = 2s_0(k_0)^{\frac{3}{2}} \left(1 - \frac{1}{k_0 + (k_0)^{\frac{1}{2}} \cdot \frac{d}{s_0}} \right) \quad (4.4)$$

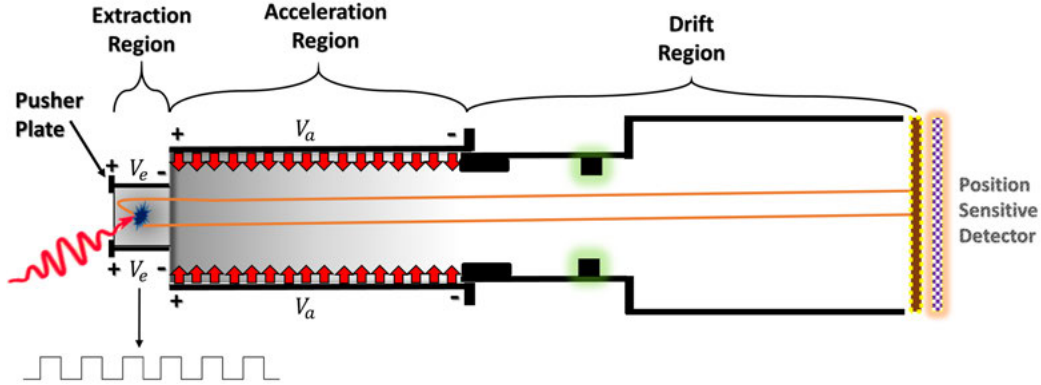


Figure 4.3: Schematics diagram of the time of flight (TOF) spectrometer.

s_0 is the length which the ions travel before entering the acceleration region, d is the length of the acceleration region, and D_o is length of the drift region. The value for the k_0 is the following:

$$k_0 = 1 + \left(\frac{d}{s_0} \right) \cdot \left(\frac{E_a}{E_e} \right) \quad (4.5)$$

Therefore, we can adjust the resolution of the mass spectra by adjusting the ratio of the electric field $\left(\frac{E_a}{E_e} \right)$. If an ion TOF MS is operated in this condition, the broadening of the TOF peaks reflects the initial kinetic energy of the ions. The key advantage of the Wiley-McLaren ion TOF MS is the combination of high transmission, high sensitivity, and easiness of mass-scale calibration.

Additional information on the ions, we can use a position-sensitive detector for recording the timing and hit position of each ion in *velocity map imaging* (VMI) mode. In VMI mode, one (or more) extra circular ring electrodes are added. This mode permits to determine the ion momenta gained in different fragmentation reactions. In **Paper I**, we used Wiley and McLaren's condition only, and in **Paper II**, we use VMI mode even through the information obtained through VMI mode is not discussed in the paper.

In my thesis, for the coincidence spectroscopy studies, a pulsed³ extraction voltage source is used. The electron detection triggers the pulsed extraction and starts counting the TOF of the ions.

At the FinEstBeAMS beamline, an MCP with an 80 mm active diameter Roentdek detector with HEX-anode [83] delay-line setup was used during

³Another option is a constant field, when the ionization source is pulsed.

4.3 X-ray Absorption Spectroscopy

measurements. The benefits of the setup are large imaging area, precise multi-hit timing information, and high detection rate. The detected signal is transferred to two fast sampling ADC units (proprietary fADC4 cards by RoentDek Handels GmbH) for fast data acquisition. This precise multi-hit capability helps us during the ion-ion coincidence measurements.

4.3 X-ray Absorption Spectroscopy

X-ray absorption spectroscopy (XAS) is a widely used and well-established technique to learn about the distribution of unoccupied states in the energy and space domain. Fricke and Hertz did the first studies by XAS in 1920[84, 85]. XAS is used to determine the local geometric and electronic structure of matter. As the photon is absorbed by the atom or molecule, a core-electron is excited to various unoccupied levels; the probability of relocation of the electron from a core-level to an unoccupied level purely depends on the photon energy and experimental geometry. In XAS, the low energy part of the absorption spectrum is called *X-ray Absorption Near-Edge Structure* (XANES) spectrum, as shown in the schematics representation in figure 4.4. Plenty of useful information can be gained from the XANES spectrum like the oxidation state, electronic structure of unoccupied molecular orbitals, and nature and strength of chemical bonding with the nearest neighbors[86]. The high energy part of the XAS is known as *extended X-ray absorption fine-structure* (EXAFS). The EXAFS part is connected to transitions to the continuum (~ 50 -1000 eV above the edge). EXAFS spectroscopy allows us to probe into the local structure and help us to gain information about atomic distances, as well as number and type of neighbors. Samples can be in any form, like gas, liquids, or solids. In this thesis, we applied only XANES to probe CaCl_2 nanoparticles and CaCl_2 aqueous solution (**Paper III**).

Different detection methods used to measure the XANES spectra are presented in figure 4.5. The most straightforward method giving access to the total absorption cross-section is the measurement of transmission through thin films of the sample, but this method is not applicable for many samples for soft X-rays due to the very small sample thickness required. On the other hand, the nanoparticle beam in **Paper III** would have been too dilute to record XAS in transmission mode. The most used and practical methods for measuring XAS spectra are based on the decay of the core hole by Auger or fluorescent decay. In both methods, the detected particle yield (electron, ion, or photons) is approximately proportional to the amount of core holes created. The number of core holes created directly reflect the energy dependence of the absorption coefficient. In the soft X-ray regime, the probability of Auger decay is higher than the fluorescence yield. Therefore, electron and

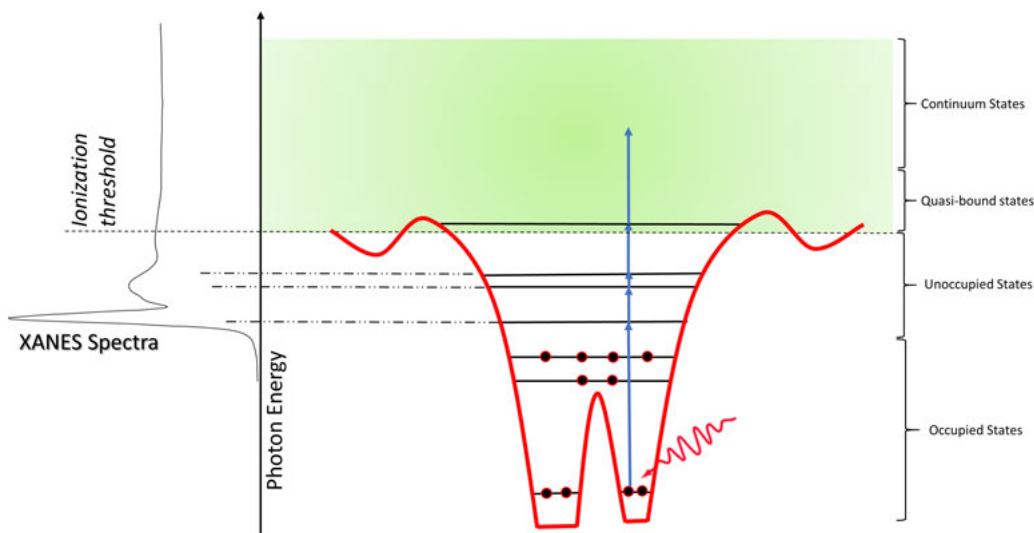


Figure 4.4: Schematics of the XANES spectroscopy.

ion yields are the more favored methods of detection. They are excellent methods to probe the surface-sensitive properties of the sample. In **Paper III**, we used XAS to characterize our system using *total electron yield* (TEY) and *partial electron yield* (PEY) detection methods. In the TEY mode all the electrons are collected, e.g. by collecting emitted electrons without energy filtering or sample drain current. In the PEY mode electrons are collected in a defined energy window, using an electron analyzer. TEY and PEY are surface sensitive methods, giving information about the few first nanometers of the sample. On the other hand, fluorescence yield is a beneficial method used to study the bulk of the material, electronically charged samples, and samples in an electromagnetic field.

4.4 Electron-Ion Coincidence Spectroscopy

Both electron and mass spectroscopy deliver valuable information about the ionized and excited molecules' relaxation [87–89] and fragmentation [90, 91]. Electron-ion coincidence spectroscopy is a combination of electron and mass spectroscopy and provides different possibilities to obtain information about different decay channels of ionized and excited molecules. Different coincident techniques are designed to probe different kinds of processes in molecules. In this thesis, the main focus is to probe sequential fragmentation processes, therefore the most suitable technique is PEPI(PI)CO. In PEPI(PI)CO, the electron detection is used as a timestamp to start the time-of-flight measurements in a mass spectrometer, and was first introduced by Frasinski and

4.4 Electron-Ion Coincidence Spectroscopy

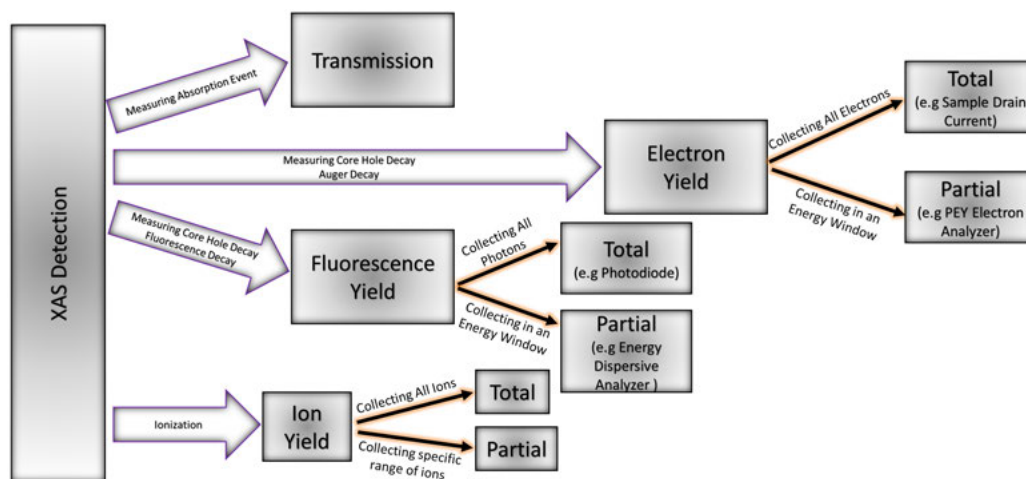


Figure 4.5: Summarizing of different detection methods mostly used to measure the XAS spectrum.

Eland in 1986 [92, 93]. Moreover, the same technique is used to detect other types of electrons (like Auger electron) instead of photoelectrons. In this scenario, the method is called AugerElectron-PhotoIon coincidence (AEPICO) spectroscopy. Regardless of which type of electron is being detected, the main principle behind the technique is the same.

As mentioned above, coincidence spectroscopy is used to monitor different decay processes in molecules. Core-excited states usually decay on the femtosecond timescale. The relaxation of the core hole states leads to doubly charged states, which are mostly very unstable and cause fragmentation by charge separation. The double ionization processes lead to bond breaking/making, and in consequence, multi-step fragmentation happens. In that case, it is important to understand the electronic relaxation processes to understand core photoionization dynamics [94]. The problem with such coincidence techniques is that they are very time-consuming. Looking for more than one electron from the same ionization or excitation event is even more challenging and slows data analysis in our kind of experimental setup. However, it can be done relatively fast with a magnetic bottle spectrometer due to its large acceptance angle. In **Papers I & II** of this thesis, we use PEPI(PI)CO to explore the sequential fragmentation and dynamics of molecules in gas-phase.

4.4.1 PEPI(PI)CO Technique and Apparatus

The coincident technique’s core idea is to measure the photoelectron with the resulting photoion(s) from an ionization event. Various research groups successfully applied this technique in different studies, from small to big

molecules [95–100].

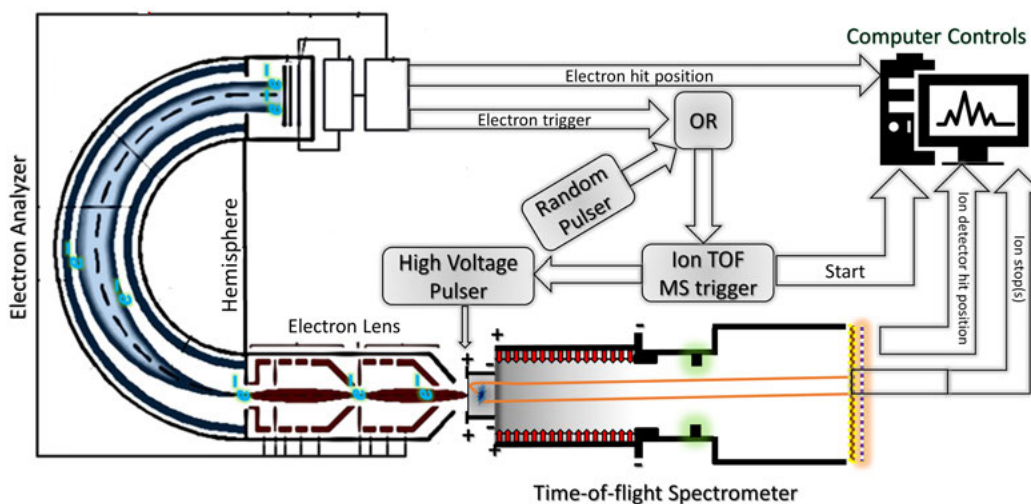


Figure 4.6: Schematic of an electron-ion coincidence measurement setup.

As the electron is detected by the electron analyzer, the signal triggers a high voltage pulse. This raises the voltage in the ion spectrometer’s extraction region, which forces positive ions to move towards the ion detector. The high voltage is retained in the extraction region for a specific time interval; mostly the time interval is longer than the flight time of the most massive ion measured in the spectrometer. For every electron detected, several ions can be measured by the ion spectrometer. Figure 4.6 shows the electron-ion coincidence setup, a combination of an electron analyzer and an ion spectrometer. Through electronic and software systems, both spectrometers communicate with each other.

The homemade software called FEBStar⁴ is used for communication between the electron and ion spectrometers. The FEBStar software’s role is to monitor and record the output of the RAD and provide a “virtual camera” interface to the user by visualizing the pattern of electron hits on X-Y coordinates. These electron hits are monitored in a specific energy window. In the FEBStar system, one of the coordinates is placed along the focal plane’s energy dispersion direction and the other along the non-dispersive direction of the electron distribution on the RAD. Thus, the energy dispersion direction coordinate is converted into electron kinetic energy, and the non-dispersive direction coordinate transformed into an image of the source area. The “SESControl” software is the primary measurement software. It can control the SES R4000 power supplies via a USB link. Setting up the

⁴Made by Prof. Edwin Kukk, University of Turku, Finland

4.4 Electron-Ion Coincidence Spectroscopy

scans of the spectra, controlling the analyzer voltages, and calibration is done through this software.

The electron spectrometer has to be set at some specific electron energy window. In the electron spectrometer's coincidence mode, we mostly used large pass energy to get a high transmission of electrons and record the whole energy range at once. The ion spectrometer's presence also affects the electron spectra resolution because of the electric field penetrating to the interaction region and even residuals fields. Moreover, we have to keep in mind as electrons are detected for specific energy windows only, and residual fields decrease electron spectrometer transmission. This enhances the chances of the false coincidences. To overcome this challenge, we have used random start pulses in addition to electron-triggered starts to estimate the effect of false coincidences to our experiment as explained in the PEPI(PI)CO data analysis chapter.

4.4.2 *CoboldPC Program Package*

Electron-ion Coincidence data can be handled and represented in many ways. In this thesis, the data analysis was done with a commercial software called CoboldPC (RoentDek GmbH) program package, and CoboldPC stands for “Computer Based Online Offline List mode Data analyzer”. CoboldPC is intended as a convenient data acquisition (DAQ) and online/offline data analysis (DAN) program. This software is very flexible because of its modular structure with elaborate data treatment.

The acquisition of coincidence datasets is also made with the CoboldPC program package. The acquired data (events) received from the DAQ hardware can be stored on the disc in a list-mode format (ListModeFile). One of the benefits of data acquired by CoboldPC is that the software stores data event by event to facilitate users to re-run analysis offline after the experiment. The size of list-mode files depends on the number of events and the number of coordinates per event, for example six days of beamtime resulted in average 150 GB of data. The detailed working of the CoboldPC software is present in manual [101]. During acquisition or reading of an offline data file, the “DataEvent-array” is very important because that array is related to coordinates, which is already defined in the CCF file. The primary function of this array in the DAQ and DAN modules is to protect the raw data. In our case, coordinates⁵ and DLL files are already defined. During the analysis, we mostly defined different spectra with different conditions on it, like filtering out a coincident electron spectrum for a particular mass peak or TOF mass

⁵A variable used for the data transfer between the main program and the DAQ and DAN modules

spectrum region as done in **Paper I**.

PEPIPICO Data Analysis

5.1 *Basic PEPICO Data Handling*

This chapter discusses how the acquired PEPICO dataset was treated and how much information we can extract from such a dataset and how it is done.

Charge separation of the doubly ionized core holes results in fragmentation in many different ways, and a significant amount of kinetic energy is released in the process. Due to charge separation and conservation of momentum, the fragmented charged ions have prominent axial velocity in opposite directions before extraction. Thus, the TOF of the same ions changes, and the flight time distribution in the spectrum is broadened. First, this is considered a disadvantage, and the development of the coincidence technique then turned this into an advantage. The PEP(PI)CO measurement dataset consists of recorded events instead of continuous measurements. Every electron detection will act as a timestamp of multiple ions. That will help us to correlate every electron with multiple ions created by the same ionization event.

The correlation of multiple ions can be expressed in the two-dimensional (2D) maps (slower coincident ion vs. faster coincident ion), as shown in figure 5.1. The coincident ions with initial axial velocity, which increase or decrease the ions' TOF appear as “*cigar-shaped*” tilted pattern with a negative slope on a 2D map. These cigar-shaped tilted patterns give us much information about the fragmentation dynamics of the molecule, for example how much kinetic energy is released during the fragmentation and how sequential fragmentation takes place step by step, as well as many other aspects of the fragmentation dynamics [102–106].

5.2 *Dissociation Mechanisms*

In this section, some fragmentation mechanisms are introduced and discussed in detail.

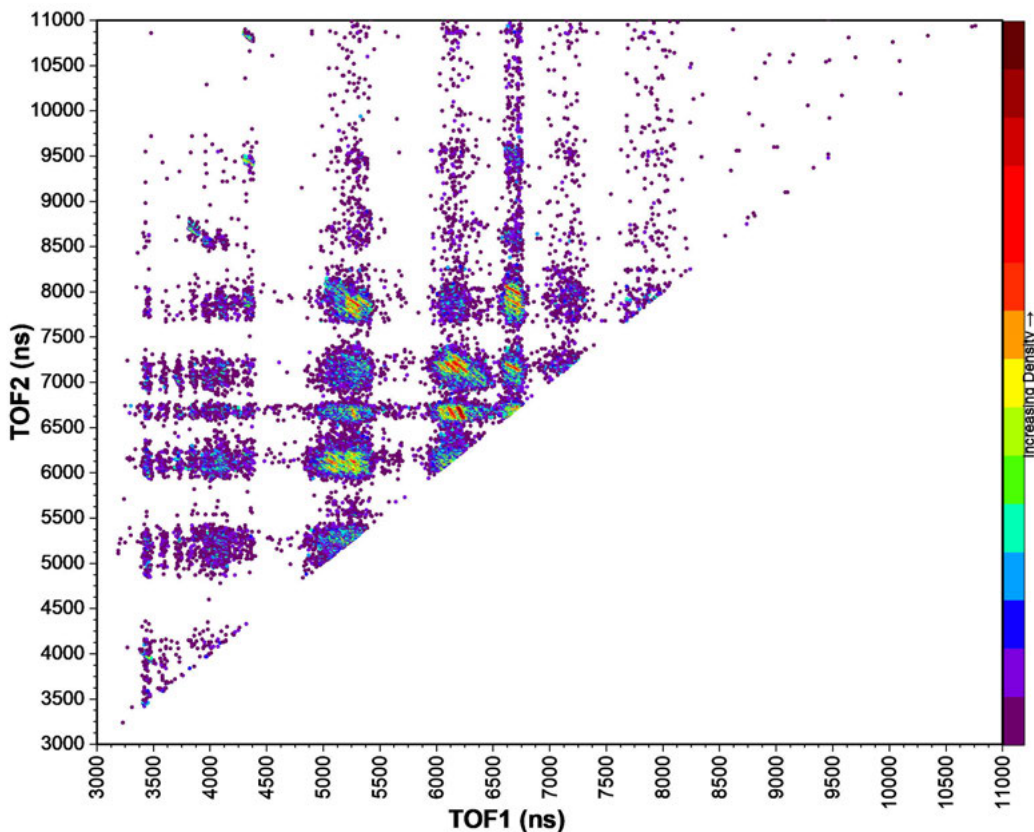
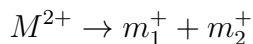


Figure 5.1: Example of PEPIPICO 2D map of ortho-aminobenzoic acid molecule.

5.2.1 *Two-Body Dissociation*

Two-body dissociation is a straightforward way of dissociation of doubly charged valence states. In two-body dissociation, the doubly charged parent ion fragments into two singly charged cations m_1^+ and m_2^+ :



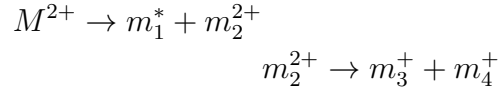
The total momentum of the fragmentation is the vector sum of the momentum of each fragment. In this case, it is zero plus the momentum of the parent ion's thermal, rotational, and vibrational movement. In reality, the momentum given to the fragments by electrostatic repulsion is much larger than the molecular thermal movement at room temperature. In **Paper I & II**, the vapor pressure is small, so we heated the sample for evaporation. That is why pre-ionization thermal movement is large and tilted pattern looks more broadened. In most of the cases we ignore internal movements (thermal, vibrational and rotational) of molecules and focus to electrostatic repulsion of fragments. The positive ion TOFs are consequently anticorrelated.

5.2 Dissociation Mechanisms

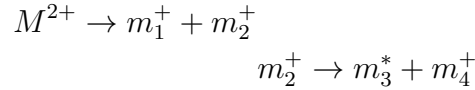
5.2.2 Many-Body Dissociation

Many-body dissociation of a dication means charge separation of the parent ion into two cations plus one or more neutral fragments. There are three different kinds of three-body dissociation mechanisms, producing two cations and one neutral fragment [56]. These three types of three-body dissociation processes are the following[107]:

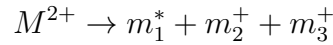
(1) *Deferred charge separation*: In this type of fragmentation, the neutral fragment is released first, after which the charge separation happens.



(2) *Secondary decay*: In this type of fragmentation, the neutral fragment appears after the charge separation.

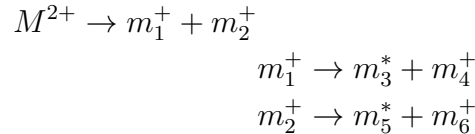


(3) *Concerted dissociation*: In this type of fragmentation, the neutral fragment is emitted simultaneously with the charge separation:

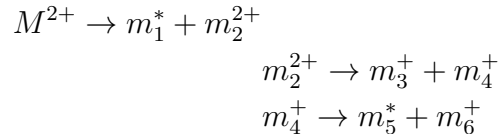


In three-body dissociation, there is a possibility of many-body dissociation producing a cation pair together with two or more neutral fragments. Three examples are given below.

(4) First, there is a secondary decay followed by further dissociation with neutral fragments:



(5) First, there is a deferred charge separation followed by secondary decay.



(6) In the first two-steps, there is no charge separation, only ejection of neutral fragments, and in the third step, the deferred charge separation of the doubly charged fragment occurs:

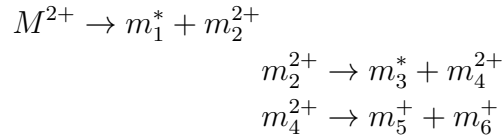


Figure 5.2 represents one more time the sequential fragmentation mechanisms during the charge separation.

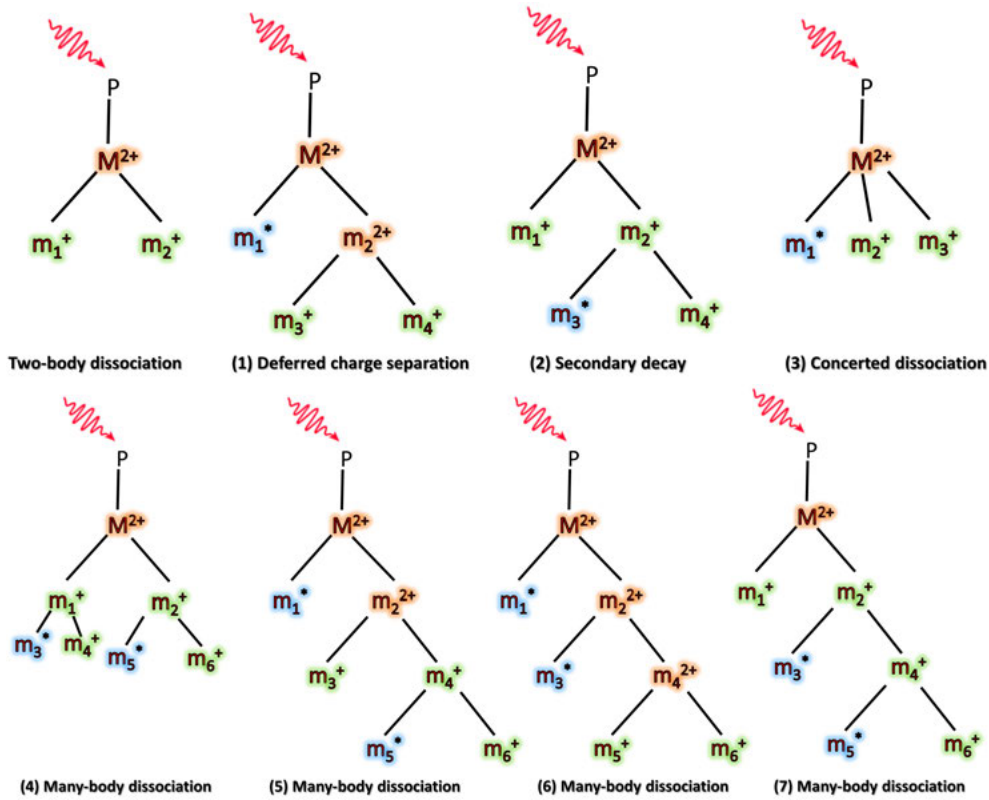


Figure 5.2: Schematic illustration of the sequential fragmentation mechanisms during the charge separation of doubly charged ions.

5.3 Pattern Slope Calculation

In all the fragmentation processes described in the previous section of this chapter, charged fragments often get a large amount of the released kinetic energy. The released kinetic energy is reflected by the length of the pattern

5.3 Pattern Slope Calculation

in the 2D coincidence map. However, the equation for the KER depends on the fragmentation mechanism. In this thesis, we did not calculate the KER of the fragments.

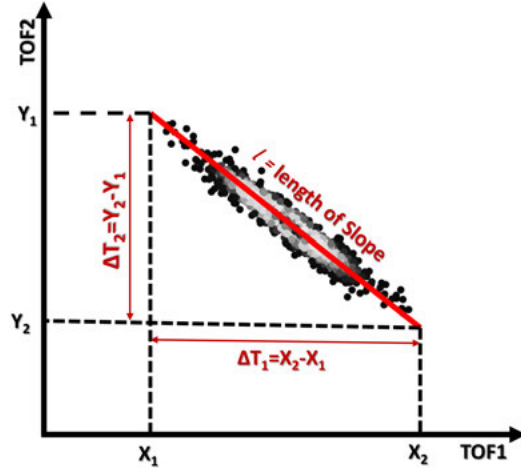


Figure 5.3: A schematic PEPICO pattern indicating the calculation of slope and length of the slope.

The experimental slopes (see figure 5.3) compared with the calculated slopes [98, 99, 108] of different patterns gives information about the various fragmentation mechanisms. Let us define the experimental and calculated slopes of different fragmentation mechanisms. The slope calculation is also demonstrated for a specific coincidence pattern in figure 5.3. The experimental slope (k) is defined as follows.

$$Slope(k) = \frac{\Delta T_2}{\Delta T_1} \quad (5.1)$$

Here ΔT_1 and ΔT_2 are the flight time of the slower and faster ions, respectively.

The equation of motion in the first approximation of flight time of charged particles is:

$$\frac{\partial T}{\partial v_a} = -\frac{1}{a} \quad (5.2)$$

Here a is the ion's acceleration and v_a is the axial velocity in the TOF system. The acceleration can be calculated from the following equation.

$$a = \frac{qU}{dm} = C \frac{q}{m} \quad (5.3)$$

Here d is the distance, and U is the voltage applied to the extraction region of the TOF system. The q/m is a charge to mass ratio of the molecule, and

C is a constant.

The spread of the initial axial velocity of the ion is:

$$\Delta v_a = 2v_a \quad (5.4)$$

Equation 5.3 and 5.4 give the resultant flight time spread:

$$\Delta T = -C \frac{m}{q} 2v_a \quad (5.5)$$

According to the law of conservation of momentum, in two-body dissociation, the momenta of two charged fragments are equal but opposite in direction:

$$m_1 v_1 = -m_2 v_2, \quad (5.6)$$

where m and v are the mass and velocity of the first and second fragments. By inserting the equation 5.6 to 5.5, we get the following equations:

$$\Delta T_1 = -C \frac{m_1}{q_1} 2v_a, \quad \Delta T_2 = -C \frac{m_2}{q_2} 2v_a \quad (5.7)$$

In two-body dissociation, the charge separation produces two cations, and the resulting slope value is:

$$\frac{\Delta T_2}{\Delta T_1} = -\frac{q_1}{q_2} \quad (5.8)$$

and if $q_1 = q_2$ we get a slope value of -1.

The slope calculation of the three-body dissociation is more complicated than two-body dissociation. If there is a concerted dissociation, no universal equation exists for this kind of dissociation due to the distribution of momenta into three fragments. However, it is possible to calculate the slope value for sequential fragmentation mechanisms like the deferred charge separation and the secondary decay.

(1) *Deferred charge separation:*

The KER in the first step is minimal compared to the second step since the model assumes that the kinetic energy is mostly gained to the charged fragments since there is a Coulomb repulsion between them. Let us assume that the fragments denoted as m_3^+ and m_4^+ have TOF spreads of ΔT_3 and ΔT_4 of the slower and the heavier ion, respectively. The slope equation is the same as for the two-body dissociation, i.e. the slope is -1 if fragments are both singly charged.

$$\frac{\Delta T_4}{\Delta T_3} = -\frac{q_3}{q_4} \quad (5.9)$$

5.3 Pattern Slope Calculation

(2) *Secondary decay:*

In this fragmentation mechanism, the slope value is influenced by the point of ejection (first/second step) of the heavier coincident cation. As we assumed that the KER mostly goes to charged fragments, the velocities of the fragments produced in the second step are:

$$v_3 \approx v_2 \quad \text{or} \quad v_4 \approx v_2 \quad (5.10)$$

The spread in flight time in the second step of fragmentation is:

$$\Delta T_2 \approx -C \frac{m_4}{m_2} \frac{m_1}{q_2} 2v_1 \quad (5.11)$$

During the secondary decay, the charge separation happens during the first step into two charged fragments m_1 and m_2 and then one of charge fragment like m_2 further fragmented into m_3 and m_4 . Assuming that m_4 is the heavier cation, the slope is then:

$$\frac{\Delta T_4}{\Delta T_1} = -\frac{m_4 q_1}{m_2 q_4} \quad (5.12)$$

And if the m_4 is a lighter cation, the slope is:

$$\frac{\Delta T_1}{\Delta T_4} = -\frac{m_2 q_4}{m_4 q_1} \quad (5.13)$$

Equation 5.12 indicate that the slope will always be less than -1 (less steep), and equation 5.13 the slope will always be more than -1 (steeper).

For four-body dissociation including secondary decay and deferred charge separation shown in figure 5.2(4), (5), and (7), the slopes are measured like in three-body dissociation. In fragmentation pattern (5) the majority of the KER goes to the cation fragments; and the slope is defined as:

$$\frac{\Delta T_6}{\Delta T_3} = -\frac{m_6 q_3}{m_4 q_6} \text{ for } m_3 < m_6 \quad \text{and} \quad \frac{\Delta T_3}{\Delta T_6} = -\frac{m_4 q_6}{m_6 q_3} \text{ for } m_3 > m_6 \quad (5.14)$$

The fragmentation process (7) is described as above in equation 5.14, only ΔT_3 , m_3 and m_4 is replaced by ΔT_1 , m_1 and m_2 respectively. The slope of the fragmentation mechanism (6) is the same as the fragmentation mechanism (2):

$$\frac{\Delta T_5}{\Delta T_6} = -\frac{q_6}{q_5} \quad (5.15)$$

For fragmentation mechanism (4) in figure 5.2, after the parent ion's charge separation, the cations release one neutral fragment from each separated fragment in the second step. The resulting slope equation is the following:

$$\frac{\Delta T_4}{\Delta T_6} = -\frac{m_6 m_1}{m_4 m_2} \text{ for } m_6 < m_4 \quad \text{and} \quad \frac{\Delta T_4}{\Delta T_6} = -\frac{m_4 m_2}{m_6 m_1} \text{ for } m_6 > m_4 \quad (5.16)$$

In **Papers I & II**, we were applying the above slope calculation models for three-body and four-body dissociation based on the assumption that the charged fragments gained the maximum amount of KE compared to neutral fragments. As the fragmentation mechanism gets more complicated, this model's accuracy is also reduced.

5.4 Challenges in Coincidence Spectroscopy Technique

The length of the slope tells how much kinetic energy is released during the dissociation process. A calculation for a PEPIPICO pattern of slope k and length l is also demonstrated in figure 5.3. In concerted fragmentation of the molecule, when a molecule fragments into several fragments in an explosion-like manner, the pattern appears in 2D maps like an irregular shape. The momentum is distributed over all the fragments. Therefore, in 2D maps, it is challenging to recognize between the sequential or concerted fragmentation of the molecule, especially in the large molecule when there is massive fragmentation.

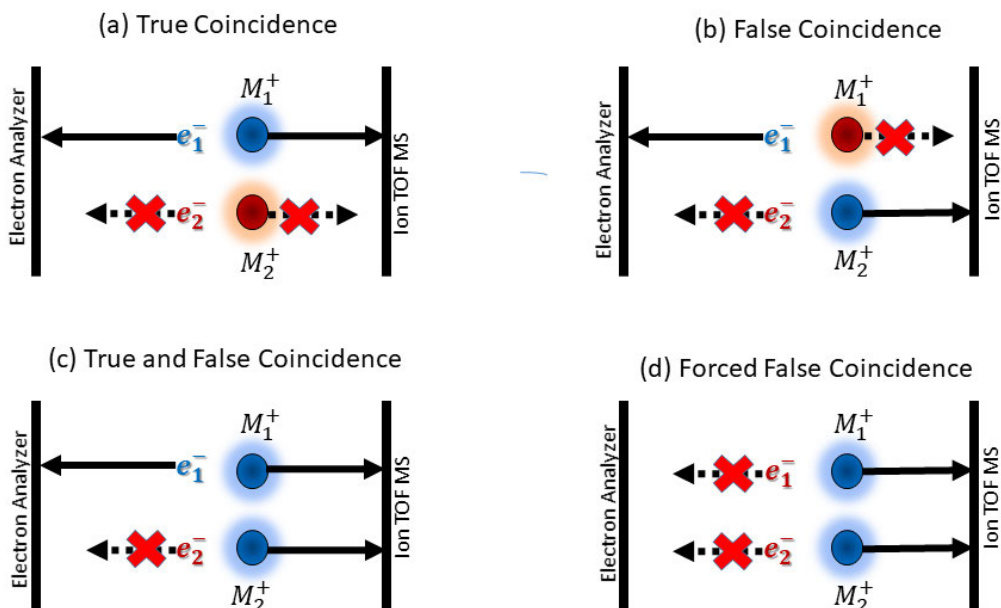


Figure 5.4: Schematic illustration of the source of true and false coincidences in two molecule ionization. Particles shown in blue reached the detector but the red ones did not.

Another challenging part of the PEPIPICO measurements is to minimize

5.4 Challenges in Coincidence Spectroscopy Technique

the outcome of the false coincidences. If more than one molecule is ionized and extracted from the interaction region, then the possibility that the detected electron is not from the same ionization event increases. These kinds of coincidence events are called “false” coincidences. The reason behind false coincidences is the difference in transmission between an electron and ion spectrometers. Figure 5.4 shows a simplified representation of “false” and “true” coincidences, but in a real scenario, the situation is even more complex. These false coincidences increase not only the background and noise of the coincidence data, but also contribute if the two ionization events are close in time, the TOF of the ion matches with the peak in the TOF spectrum of real ions. The ionization amount in the interaction chamber depends on different aspects like photon flux and molecular number density. In any coincidence dataset there are three different kinds of events recorded simultaneously, shown in figure 5.4(a),(b), and(c). There are different statistical ways to remove the false coincidences from the analysis. One way to decrease the false coincidences is to decrease the ionization rate during the experiment i.e. in our experiments fewer than ~ 20 to 30 counts/s decreases the number of events happening simultaneously. Another option with a low counting rate method is to collect data using a random trigger (a type of event created by that is shown in figure 5.4(d)) and subtract that from all coincidence data [109]. This method is statistically beneficial for removing false coincidences from coincidence data sets [98]. The electron signal from an electron spectrometer and a pulse from a random generator are connected through an OR connection, as shown in figure 4.6. The difference in electron triggered, random triggered, and true (after random subtraction) events TOF mass spectra are shown for ortho-aminobenzoic acid in figure 5.5.

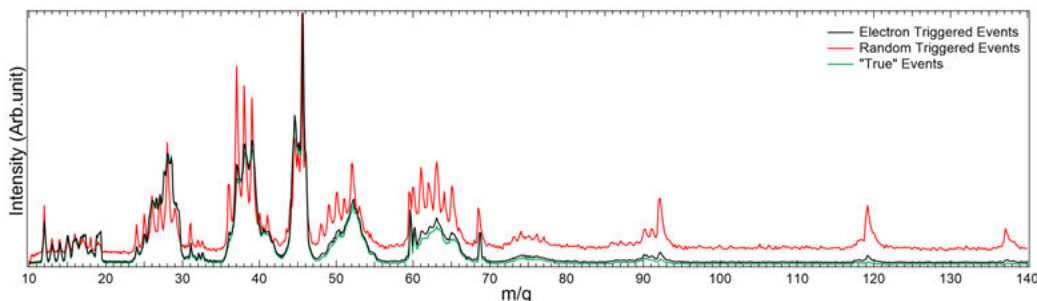


Figure 5.5: TOF mass spectra, the difference between the electron, random triggered, and true (after random subtraction) events in ortho-aminobenzoic acid.

These methods of removing false coincidences are just approximations, and do not eradicate all false coincidences.

In **Paper I**, we used only the low counting rate method to avoid false coincidences. In **Paper II**, we used both low counting and random trigger subtraction methods to eliminate false coincidences as much as possible.

Research Objectives and Results

The main focus of the chapter is to discuss the objectives and execution of the studies in **Papers I-III** and to summarize the results.

6.1 Photofragmentation of Molecules - Papers I & II

In the **Paper I & II**, the main objective was to study the core-ionization-induced fragmentation of the benzene-ring-based biologically important organic molecules (Avobenzene (AVOB) and Ortho-Aminobenzoic Acid (o-ABA)). The valence ionization of the molecules was also studied to some extent. Molecular fragmentation was studied by ionizing the core electrons (C1s and O1s) and measuring the photoelectrons' kinetic energy in coincidence with TOF measurements of corresponding photoions. The recorded ionization events are plotted as coincidence 2D maps to identify the coincident fragments. These coincident fragment pairs help to understand fragmentation pathways, intensities of different fragmentation channels, and KER distribution¹ during fragmentation, as described in chapter 5. Besides that, the PEPI(PI)CO data help to understand the role of the first ionization site and the molecular geometry in determining the fragmentation channels.

6.1.1 Photofragmentation of Avobenzene - Paper I

The AVOB molecule is a large organic molecule with two benzene rings connected by a bridge. It has two isomers (enol and keto form) simultaneously existing in equilibrium[110, 111]. The photofragmentation of AVOB after core-ionization and subsequent Auger decay into a double charged parent ion has been studied. If we think about the fragmentation of the doubly charged ion, one of the easiest ways of charge separation is by a simple bond

¹In this thesis, we mostly described the qualitative ways to discuss KER distribution, not quantitative.

cleavage into two singly charged fragments. For such a large molecule, there are many possible bond cleavages, leading to many possible channels, resulting in a complicated fragmentation pattern. Charge separation is a vital step in the fragmentation, and it can happen at the first stage or later, and ultimately the number of total fragments ejected can be two or more. A simplified picture of some doubly charged sequential fragmentation channels is shown in figure 5.2, and several specific fragmentation channels for AVOB are shown in **Paper I**.

Based on the results of **Paper I**, we concluded the following:

- Based on the calculation of O1s electron spectra of enol and keto forms compared with experimental coincident electron spectra, we can conclude that the enol form is dominant over keto form in our gas-phase experiment.
- Valence photoionization results in photon energy-dependent fragmentation. From valence PEPICO analysis, the low binding energy outermost orbitals are from the benzene rings, and orbitals around the bridge have higher binding energy.
- The TOF mass spectrum’s sharp peaks indicate the presence of stable doubly charged ions (like 147 amu). This finding is further confirmed by the ion TOF MS detector images, which show that the hit positions of these ions are concentrated in the center of the detector.
- The elemental selectivity is negligible, and the mass spectra look similar, no matter whether the ionization has happened at C1s or O1s. The core-shell ionization leads to a massive fragmentation of the molecule, with little site-selectivity relative to fragments’ production.
- Even after the massive fragmentation after molecular core-ionization, the benzene ring stays intact because the fragments with $m/q > 72$ are a significant part of total yield.
- The ion-ion momentum correlations² allow us to identify different fragmentation channels and use the different slope models. Based on the slope analysis, we reconstructed different sequential fragmentation pathways for some heavy ion-ion pairs.
- In the case of deferred charge separation, before the charge separation steps, the ejection of a neutral fragment has mostly occurred in the outer arms of the AVOB molecule.

²Specially at region C of PEPICO map, shown in figure 6.2(b)

6.1 Photofragmentation of Molecules - Papers I & II

- There is a possibility of different geometries (isomers) of fragments after fragmentation, which we cannot be distinguished with the help of a mass spectrometer that measures only the charge-to-mass ratio of a fragment. Therefore, the geometries shown in the proposed mechanisms of **Paper I** are tentative.

Presence of different isomers (Enol or Keto)

AVOB has two stable isomers enol and keto, but calculations showed that the keto form has a slightly lower energy in gas-phase. However, the accuracy of the calculation did not allow us to firmly conclude which form would be of lower energy. A comparison of calculated electron spectra of both forms with the experimental coincident electron spectra was done to know which isomeric form we are ionizing during the measurements. The coincident valence, C1s and O1s spectra of AVOB are shown in figure 6.1.

The valence electron spectrum shows two different characteristic regions. The region with binding energy less than 10 eV is more compatible with the enol form. Comparing the shape of the calculated and experimental spectrum did not give us a clear idea about which isomeric form is present.

The C1s electron spectrum also has two peaks from the different chemical environments of the carbon atom. The higher binding energy peak belongs to C=O and C-O, and lower binding energy peak belongs to an alkyl group or a benzene ring. By comparing the calculated and experimental electron spectrum, we can not conclude even here, which isomeric form is more dominant.

The O1s electron spectrum also has two peaks from different chemical environments. The small peak towards the lower binding energy side is due to the ionization of C=O, and the other peak is due to the ionization of C-O-C and C-OH. By comparing the calculated and experimental spectral features, it is clear that the enol form of AVOB is dominating over the keto form, as the specific environment of the C-OH presents only in the enol form of AVOB. There are also signs of site-selectivity relative to ion production found by breaking down the electron spectra with respect to specific mass peaks.

Photofragmentation of large organic molecule

The AVOB molecule is one of the heaviest molecules studied until now using electron-ion coincidence spectroscopy. The PEPIPICO map of the AVOB molecule is shown in figure 6.2.

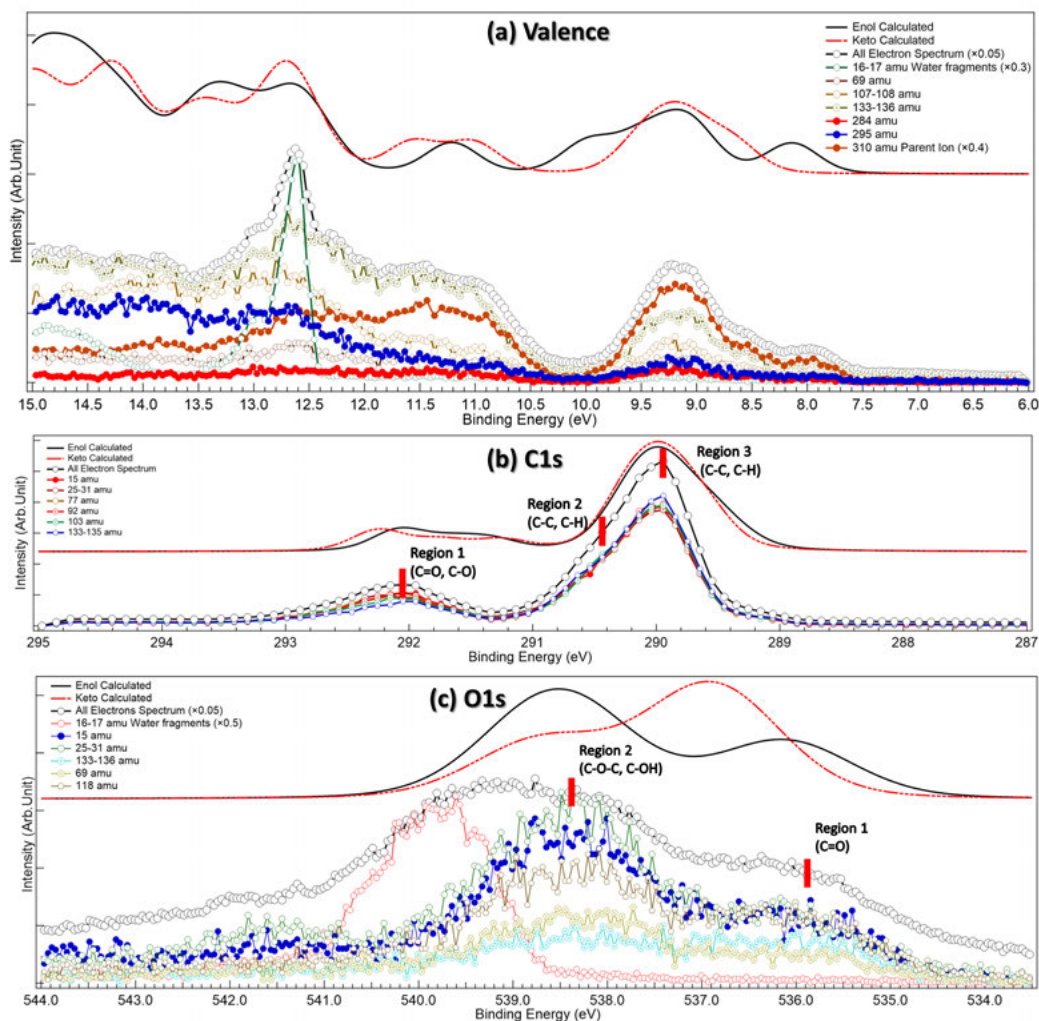


Figure 6.1: The coincident electron spectra of valence (a), C1s (b), and O1s (c) are shown. The experimental all-electron spectra are shown in black color. All other curves in different colors are electron spectra curves for specific mass fragment peaks. The red dashed and solid black curves with some offset are calculated electron spectra of keto and enol form. The calculated curves are obtained from the convolution of calculated orbital energies with 0.5 eV Gaussian and 0.1 eV Lorentzian for better visualization. (From Abid A. R. *et al.* (2020), *J. Phys. B: At. Mol. Opt. Phys.*, **53**, 244001, pp.4-7. Reproduced under permission CC-BY 4.0.)

A large number of cation pairs are found in the coincidence map. We divided the PEPICO maps into three different regions (A, B, and C). The cation pairs found in the coincidence map is from three-body and many-body dissociations. In principle, every distinctive island on the map is from different pairs, but for such a large molecule some islands may be formed by

6.1 Photofragmentation of Molecules - Papers I & II

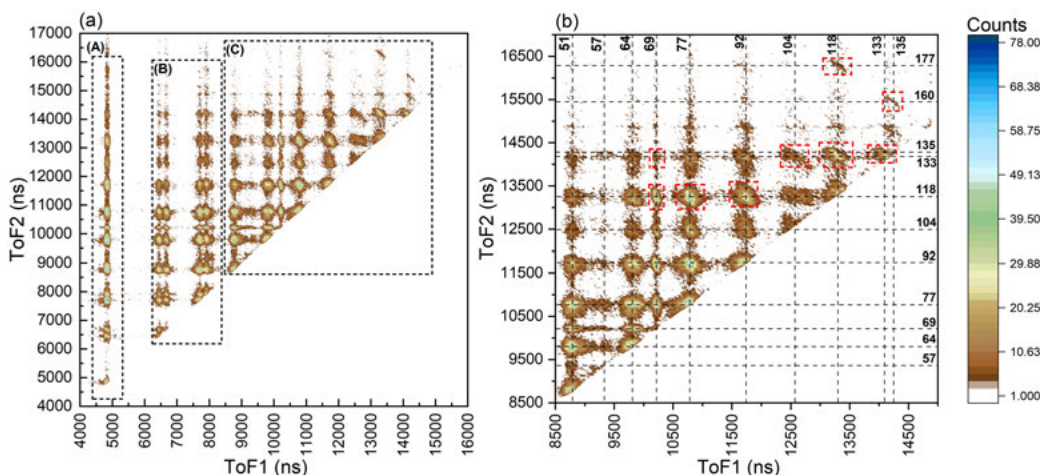


Figure 6.2: (a) Full PEPIPICO map of AVOB after C1s ionization. The map is divided into three regions, A, B, and C. (b) Enlarged Region C of the PEPIPICO map. The vertical and horizontal lines show the specific masses on both sides. The red boxes indicated the specific coincident ion pairs discussed in **Paper I**. (From Abid A. R. *et al.* (2020), *J. Phys. B: At. Mol. Opt. Phys.*, **53**, 244001, pp.8. Reproduced under permission CC-BY 4.0.)

ion-pairs created by two different pathways. In **Paper I**, we proposed some of the mechanisms by simple bond cleavage, but in reality, there are different internal bond breaking/making and rearrangements, also happening like McLafferty rearrangements, elimination processes, and hydrogen transfers.

In the AVOB C1s coincidence map, we can see different unclear and blurred coincidence pairs in regions A and B from small fragment pairs that indicate different overlapping mechanisms and release of different neutral fragments, which decrease the ion-ion momentum correlation. In region C, the large fragment pairs have significant ion-ion momentum correlations, and during analysis, we mostly emphasize this region. The comparison between the experimental slope and calculated slope³ indicates the feasibility of different proposed fragmentation mechanisms. The charge can transfer to either fragment during the fragmentation, but it is usually observed that charge transfer will happen mostly to large fragments as this tends to be energetically favourable. The charge transfer depends on the delocalization efficiency. In some fragments, we also have a possibility of different number of hydrogens, which makes maps unclear.

Moreover, in a model described by Eland *et al.* [112], the rapid charge ex-

³As described in the chapter 5 of thesis.

change happens within a so-called charge exchange zone, in which the charge is delocalized and shared by all parts of the molecule. In short, the charge is jumping around all parts of the molecule until the bond distance has become too large for any more charge exchange between the separating fragments. These bond distances increase faster with double ionization compared to single ionization due to Coulombic repulsion. In AVOB, the charge is mostly retained in a large fragment. Before moving out of the charge exchange zone the charge stays longer in large fragments compared to small fragments and moreover, the energy is minimised when charge is within the large fragment.

6.1.2 Photofragmentation of Ortho-Aminobenzoic Acid - Paper II

Aminobenzoic acid is an organic molecule consisting of a benzene ring with a carboxyl ($\text{C}=\text{O}$) and an amine (NH_2) functional group attached at different positions, resulting in so called positional isomers. We studied the fragmentation of the two positional isomers, ortho- and meta-aminobenzoic acid (o-ABA and m-ABA, respectively, see figure 1.1) after core ionization and subsequent Auger decay. The doubly charged parent ion fragments through different channels. The coincident map of o-ABA after C1s ionization is presented in chapter 5, figure 5.1. We observed the positive H_3O^+ fragment with significant KE in different fragmentation channels, see figure 6.3, and **Paper II**, is mostly focused on the creation mechanisms of the H_3O^+ .

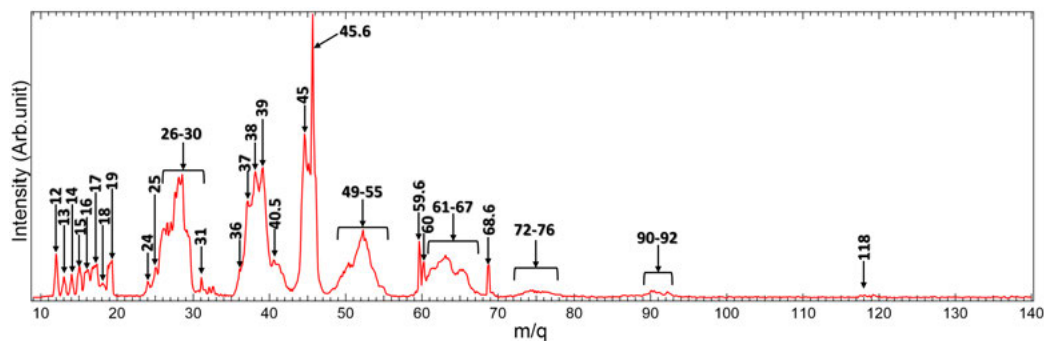


Figure 6.3: The C1s coincident TOF mass spectrum of o-ABA is shown with peaks labeled with the fragment mass in amu.

Based on the results of **Paper II**, we concluded the following:

- The comparison between the o-ABA and m-ABA mass spectra show a higher abundance of H_3O^+ for ortho-isomer. The proximity of the functional groups in the ortho-geometry requires minimum double intramolecular hydrogen transfer for the formation of H_3O^+ .

6.2 XAS of Hydrated Nanoparticles - Paper III

- MacLot *et al.* [113] explain two competing processes; the more dominant one is the Coulomb explosion leading to dissociation into two singly charge fragments, and other one is hydrogen transfer leading to stable dication in glycine. Besides these two processes in our molecule, we observed that the minimum double hydrogen transfer leads to the formation of H_3O^+ by Coulomb explosion.
- In o-ABA, the production of H_3O^+ and the doubly charged parent ion is site-selective. H_3O^+ is more abundant at C1s and least at O1s. The doubly charged parent ion is produced mostly at N1s and least at O1s.
- Several two-body and three-body dissociation channels are present, for which at least one ion is H_3O^+ . Possible fragments with slope analysis are shown in figure 6.4.
- Two different channels are identified after filtering coincident map, which produce similar fragments, namely charged 19 (H_3O^+) and 90 ($\text{C}_6\text{H}_4\text{N}^+$) with a neutral 28 (CO), and charged 29 (COH) and 90 ($\text{C}_6\text{H}_4\text{N}^+$) with a probable neutral 18 (H_2O). Relative coincidence yield of the former is almost twice compared to the latter.

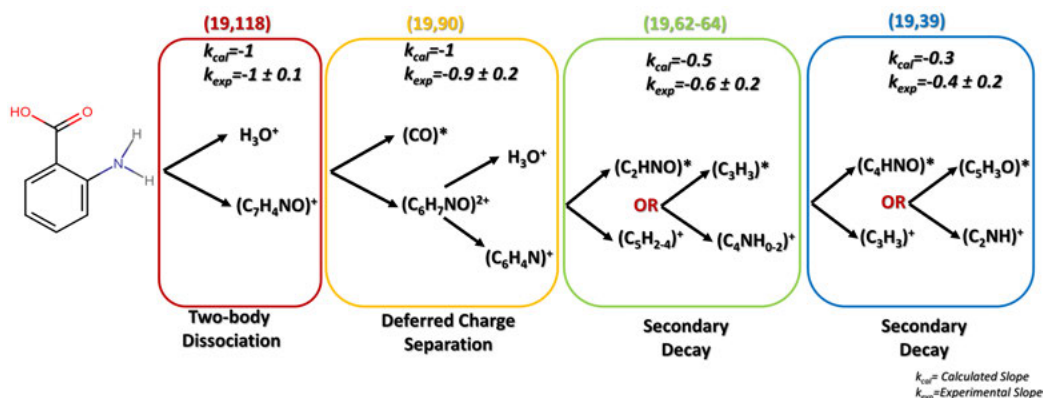


Figure 6.4: Schematics showing the dissociation channels leading to the production of H_3O^+ and second possible fragment(s) with their slope analysis.

6.2 XAS of Hydrated Nanoparticles - Paper III

In **Paper III**, the main emphasis is to understand the effect of relative humidity (RH) on biologically and atmospherically important molecules inside a water matrix system. Therefore, we selected calcium chloride (CaCl_2) salt because Ca- and Cl- comprising hydrated nanoparticles (NPs) are essential both biologically and atmospherically. The free-flying NPs are generated by

an atomizer system, as described in chapter 3. The NPs generated are in a 100 to 200 nm size regime. The hydrated NPs are partially dried in flight to create a range of relative humidity (RH) from 11% to 85%. Moreover, we also produced mixed NPs of Phenylalanine (Phe) and CaCl_2 .

The hydration properties of the CaCl_2 -NPs and mixed NPs were probed with XAS at the Ca2p, Cl2p, C1s, and O1s absorption edges.

The main idea of **Paper III** is to demonstrate the use of soft X-ray absorption spectroscopy to probe the local effect of hydration of free-flying NPs and mixed NPs.

Based on the results of **Paper III**, we concluded the following:

- From the O1s, we found out that the water is present in a distorted liquid-like state throughout the RH range investigated, and the amount of water present correlates with RH.
- We did not find any evidence of crystalline CaCl_2 but always found it hydrated at all investigated RH values. Moreover, no significant changes in the Ca2p and Cl2p XAS spectra were found, indicating small or non-existent changes in primary hydration layers with RH.
- The difference in the Cl2p post-edge structure of CaCl_2 -NPs and mixed CaCl_2 +Phe NPs indicates that the Cl^- ion is present in near vicinity of Phe. At the C1s edge, the blue shift in the continuum resonance region indicates an elongation of Phe carbon bonds from solid form to aerosolized Phe and mixed CaCl_2 +Phe NPs.

Figure 6.5 shows the simple visual schematic of hydrated CaCl_2 -NPs generated with different RH values.

Presence and state of water

The O1s XAS spectra measured help to characterize the presence and state of water in the hydrated NPs. The pre-edge feature in the XAS spectrum of water indicates the distortion in the hydrogen bonding between the water molecules. The post-edge feature indicates the presence of long-range tetrahedral order. Looking at the O1s XAS spectra at different humidity levels, it neither thoroughly looks like the solid nor liquid in all three regions (pre-edge, main-edge, and post-edge). The NP XAS spectra appear to be in between the solid and the liquid state, and no gas-phase water is present. An increase in pre-edge and a decrease in post-edge intensities is observed from high to low RH, indicating less water content at low RH and vice versa. According to estimate of Chang *et al.*[114], due to the evaporation of water in

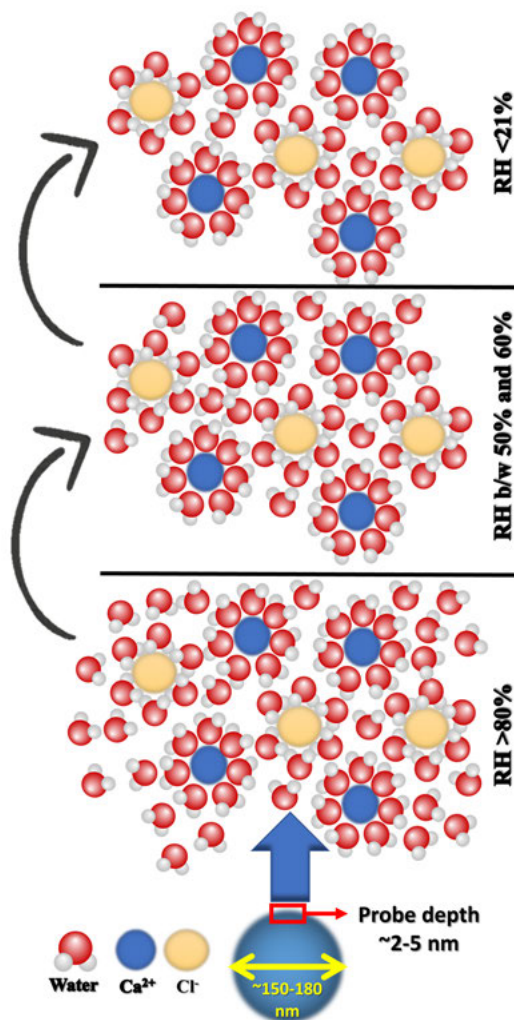


Figure 6.5: Schematic simple visualization of the hydrated CaCl_2 at different RH ranges.

the aerodynamics lens, evaporation reduces the water droplet size up to 6%, and the temperature of water falls below 193K, leaving them in a supercooled state. From that estimation, we can also conclude that our water is also in a liquid-like state. In a previous study by Kostko *et al.*[115], it was found out that similarly prepared salt (NaI) - water nanoparticles contain also ice. We did not observe ice, but one of the reasons may be the probing depth. In our case, we have approximately a probe depth of 2 to 5 nm. Therefore our experimental setup is more sensitive to the surface properties of the NP.

Research Objectives and Results

Conclusion and Outlook

Modern synchrotron radiation facilities were used to study the photoionization and photoabsorption processes to understand the initial step of radiation damage in different biologically relevant molecules. Well-established soft X-ray spectroscopy methods like electron spectroscopy, mass spectrometry, electron-ion coincidence using a hemispherical deflection analyzer and an ion time-of-flight mass spectrometer equipped with advanced position sensitive and multi-hit ion detectors, and X-ray absorption spectroscopy were used. Specialized sample delivery systems like a resistive oven for isolated gas-phase molecules, liquid-jet for samples in solution form, and atomized hydrated aerosols generated from solution carried to vacuum by an aerodynamic lens were used to introduce samples into the interaction chamber.

Photofragmentation of valence and core ionized molecules was studied, and simple bond cleavages were used to deduce different sequential dissociation processes. During many-body dissociation, the charge is mostly transferred to the heavier fragments. The mass spectra after core ionization indicate that the initial ionization site has a minimal effect on the molecules' overall dissociation pattern. We also studied the effect of the different molecular geometries of the same molecule. This is seen to significantly affect the molecules' fragmentation, as exemplified by one of the molecules exhibiting stronger double hydrogen-transfer at a specific geometry compared to the other geometry. Moreover, both molecular systems studied in **Papers I & II** have at least one benzene ring, and studies indicate that the benzene ring is hard to break even after core ionization. That is why we also observed doubly charged stable ions having mass more than a benzene ring in the mass spectra.

Hydrated inorganic and mixed inorganic-organic nanoparticles were probed using X-ray absorption at different core-levels. These hydrated nanoparticles were prepared at different relative humidity. Comparison of the X-ray absorption spectra between the solid-state (from literature) and liquid solution (from liquid-jet) was also done for hydrated nanoparticles. These compar-

isons at the different absorption edges give us information on the nanoparticles' hydration properties, solute-solvent interaction, and solvent state.

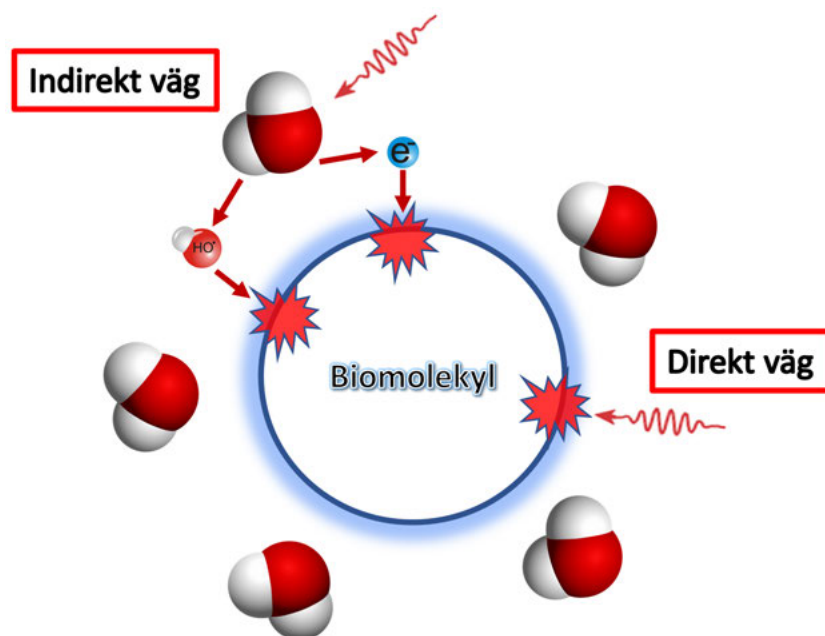
This work demonstrates the significance of high brilliance, tuneability and high stability of modern synchrotron radiation facilities to understand dilute matter systems. The work presented in this thesis (together with many previous works) also shows the usefulness of soft X-ray spectroscopic methods for studying radiation damage. In the future, these studies can act as a reference for time-resolved studies at a free-electron laser to get more in-depth knowledge about the dynamics of photofragmentation. High transmission electron analysers such as magnetic bottles can be used to study multi-electron processes, and can nowadays also be combined with ion detection. Besides that, our studies open new avenues to study the mixed organic-inorganic hydrated nanoparticles in different biologically and atmospherically relevant systems.

Populärvetenskaplig sammanfattning

Strålskador orsakade av joniserande strålning som ultraviolett strålning och röntgenstrålning på biologiskt relevanta molekyler har studerats intensivt under många årtionden. Joniserande strålning kan vara mycket skadlig, och till och med dödlig, för levande varelser. I vissa tillämpningar som strålbehandling mot cancer och röntgenbaserad medicinsk diagnostik används dock kontrollerade doser av joniserande strålning då fördelarna är större än nackdelarna. Vi skiljer ofta på två typer av mekanismer för molekyllära strålskador:

(1)*Direkt väg*: Om den joniserande strålningen påverkar biomolekylen direkt och dissocierar molekylerna i många små fragment.

(2)*Indirekt väg*: Om biomolekylen är omgiven av vattenmolekyler, kan dessa joniseras av strålningen, vilket skapar fria radikaler och långsamma elektroner, vilka skadar biomolekylen.



Schematisk bild av den direkta och den indirekta vägen för strålningsskador.

Både den direkta och den indirekta vägen för strålningsskador, vilka visas schematiskt i figur 1, är viktiga, och det behövs detaljerade studier för att förstå dem på molekylär nivå. Förutom den biologiska betydelsen av strålsskador är de också relevanta för flera andra tillämpningar som plast, färger och elektroniska apparater, och de har också atmosfärsrelevans.

I denna avhandling studeras de inledande stegen av strålningsskador med tekniker som röntgenabsorptionsspektroskopi, elektronspektroskopi, masspektroskopi och elektron-jon-jon-koincidensspektroskopi. Olika typer av prover har använts för att studera den direkta vägen (molekyler i gasfas) och den indirekta vägen (hydratiserade nanopartiklar) för strålningsskador.

I alla dessa tekniker bestrålades provet med elektromagnetisk strålning, antingen ultraviolett strålning eller mjukröntgenstrålning. Fotonenergin för båda typerna av strålning är tillräcklig för att jonisera atomer genom att slå ut en elektron från en av de yttre valensnivåerna, och med mjukröntgenstrålning kan också innerskalselektroner i atomer med lågt atomnummer joniseras. Monokromatiserad strålning från en synkrotronstrålningskälla användes för att studera valens- och innerskalsnivåer. Synkrotronstrålning är elektromagnetisk strålning av ett brett energiområde som emitteras av laddade partiklar, oftast elektroner, som när de rör sig nära ljusets hastighet accelereras av magnetfält.

När den elektromagnetiska strålningen växelverkar med materialet och frigör elektroner från olika orbitaler registreras det utgående elektronerna som funktion av deras kinetiska energi i fotoelektronspektroskopi. När sådana så kallade fotoelektroner sänds ut, lämnar de atomen/molekylen i ett joniserat tillstånd. Detta joniserade tillstånd har mycket energi och är instabilt, och elektronerna i kommer att omordna sig för att sänka sin energi. Sådana processer kallas för elektronisk relaxation. Efter jonisation av innerskalsorbital faller en elektron från en yttre valensorbital ner till innerskalsorbitalen för att fylla det hål som där bildats vid joniseringen. Denna process, kallad Augersönderfall, sänker systemets energi och leder till att en annan elektron sänds ut från någon av valensorbitalerna. Efter ett sådant Augersönderfall är de joniserade molekylerna i ett dubbeljoniserat tillstånd. I dessa molekylära joner repellerar de två laddningarna varandra, vilket leder till laddningsseparation och att den molekylära jonen fragmenterar. Dessa fragment detekteras med hjälp av masspektroskopi, där jonernas massa-till-laddningsförhållande bestäms av deras flygtid till detektorn efter en initial acceleration.

Elektron-jon-koincidensspektroskopi är en kombination av fotoelektronspektroskopi och fotojoniseringsmasspektroskopi. Eftersom elektronerna på grund av sin mindre massa är mycket snabbare än jonerna, kan fotoelektronen

fungera som en startsignal för mätningen av de bildade jonernas flygtid till detektorn. Genom detta kan vi analysera de olika fragmenten från en enda joniseringshändelse. Denna teknik hjälper oss att bättre förstå dynamiken i molekylernas fotofragmentering efter jonisering.

Vid röntgenabsorption mäts det emitterade elektronutbytet som en funktion av fotonenergin, och det är en kraftfull teknik för bestämning av materiens lokala geometriska och elektroniska struktur på atomär nivå.

Både den direkta och den indirekta vägen bidrar till strålskador på molekyllär nivå. Därför behövs en mikroskopisk förståelse av dessa molekyler, deras elektroniska struktur och joniseringsprocesser. Biomolekyler har ofta flera isomerer med olika struktur och konformation, och ett av de spännande perspektiven i molekyllär fysik är att studera hur egenskaper varierar mellan isomerer. De kan också ha olika molekyllära strukturer i gasfas, i lösningar och som fasta ämnen. Många intressanta aspekter i dessa biologiskt relevanta molekyler motiverade oss att studera förändringar i fotofragmenterings- och fotoabsorptionsprocesserna kopplade till små strukturella variationer i molekylerna.

Två organiska molekyler, avobenson och aminobensoesyra, studerades i gasfas med avseende på fotofragmenteringsdynamik efter valens- och innerskalsjonisation. Vi fann bland annat att molekylerna fragmenteras stegvis i många mindre fragment efter jonisation, att vid bildande av flera fragment överförs laddningen mest till de större fragmenten, att fragmentering efter innerskalsjonisation är oberoende av på vilken atom den initiala jonisationen skett, samt att variation i den molekyllära geometrin påverkar dissociationsskanalernas relativa betydelse.

För hydrerade oorganiska och blandade oorganiska-organiska nanopartiklar studerades både direkta och indirekta strålskador med hjälp av röntgenabsorption vid olika innerskalsnivåer. Hydratiserade nanopartiklar med varierande vattenhalt framställdes vid olika relativ fuktighet. Jämförelse av röntgenabsorptionsspektra för hydratiserade nanopartiklar, och motsvarande material i fast form och i vattenlösning vid de olika absorptionskanterna gav oss information om nanopartiklarnas hydratiseringsegenskaper, samt jonvatten-växelverkan i nanopartiklarna.

Detta arbete demonstrerar betydelsen av de moderna synkrotronstrålningsanläggningarnas höga briljans och stabilitet samt möjligheten att variera fotonenergi för att förstå molekyllära system och processer. Tillsammans med många tidigare arbeten visar arbetet som presenteras i denna avhandling också på nyttan av mjukröntgenspektroskopiska metoder för att studera

strålskador på molekylär nivå.

I detta arbete utforskades också nya fenomenen förknippade med hur parallellt med molekylär fragmentering nya bindningar bildas. Vi studerade hur hydroniumjoner bildades i en process involverande minst två väteatomer och en OH-grupp, och hur detta varierade mellan olika molekylära isomerer.

Som så ofta i forskning väcker våra resultat ännu fler frågor, som till exempel olika rotamerers betydelse för den dubbla väteöverföringen och sambandet röntgenabsorption och relativ fuktighet i nanosystem. Detta arbete utgör därmed bara ett litet bidrag i vårt utforskande av naturen.

Bibliography

- (1) E. Constable, *Comprehensive coordination chemistry II: from biology to nanotechnology*, Elsevier, Amsterdam, 2003.
- (2) J. E. Penner-Hahn, in *Encyclopedia of Life Sciences*, John Wiley & Sons, Ltd, Chichester, UK, 2005.
- (3) J. C. Lindon, G. E. Tranter and D. W. Koppenaal, *Encyclopedia of Spectroscopy and Spectrometry*, Academic Press, Amsterdam, 2016.
- (4) J. Yano and V. K. Yachandra, *Photosynthesis Research*, 2009, **102**, 241–254.
- (5) J. Evans, in *X-Ray Absorption Spectroscopy for the Chemical and Materials Sciences*, John Wiley & Sons, Ltd, Chichester, UK, 2017.
- (6) J. W. Smith and R. J. Saykally, *Chemical Reviews*, 2017, **117**, 13909–13934.
- (7) L. E. Ballentine, *Quantum Mechanics*, World Scientific Publishing, Singapore, 2nd, 2014.
- (8) N. Zettili and I. Zahed, *American Journal of Physics*, 2003, **71**, 93–93.
- (9) D. Griffiths and D. Schroeter, *Introduction to quantum mechanics*, Cambridge University Press, Cambridge, 3rd, 2018.
- (10) R. M. Eisberg and R. Resnick, *Quantum physics of atoms, molecules, solids, nuclei and particles*, John Wiley and Sons, New Delhi, 2nd, 2017.
- (11) A. Streitwieser, ACS Symposium Series, American Chemical Society, 2013, vol. 1122, pp. 275–300.
- (12) G. N. Lewis, *Journal of the American Chemical Society*, 1916, **38**, 762–785.
- (13) A. Haaland, *Molecules and Models: The molecular structures of main group element compounds*, Oxford University Press, Oxford, 2012.
- (14) E. A. William H. Brown Brent L. Iverson, *Organic Chemistry*, Cengage Learning, Boston, MA, 7th, 2013.
- (15) A. B. P. Lever, *Journal of Chemical Education*, 1972, **49**, 819.
- (16) B. B. Miburo, *Journal of Chemical Education*, 1998, **75**, 317.

BIBLIOGRAPHY

- (17) G. L. Miessler and D. A. D. A. Tarr, *Inorganic chemistry*, Pearson Education, New York, 7th, 2004.
- (18) J.-L. Calais, *International Journal of Quantum Chemistry*, 1976, **10**, 552–553.
- (19) N. L. Allinger, *Molecular structure : understanding steric and electronic effects from molecular mechanics*, Wiley-Blackwell, Oxford, 2010.
- (20) Y. Jean, F. Volatron and J. K. Burdett, *An introduction to molecular orbitals*, Oxford University Press, Oxford, 1993.
- (21) J. E. Lennard-Jones, *Transactions of the Faraday Society*, 1929, **25**, 668–686.
- (22) R. Chang and K. A. Goldsby, *General chemistry : the essential concepts*, McGraw Hill, New York, 7th, 2014.
- (23) A. C. Hurley, *Electron correlation in small molecules*, Academic Press, London, 1977, vol. 42.
- (24) H. Straw, S. Walker, J. Burdett, D Phillips, K. Salisbury, H. Walker and P. Sherwood, *Spectroscopy: Volume Three*, ed. B. P. Straughan and S. Walker, Springer International Publishing, Cham, 1976.
- (25) V. Schmidt, *Electron Spectrometry of Atoms using Synchrotron Radiation*, Cambridge University Press, Cambridge, 1997.
- (26) B. H. Bransden and C. J. Joachain, *Physics of atoms and molecules*, Prentice Hall, Harlow, 2nd, 1983.
- (27) S. S. Wilson, *Handbook of molecular physics and quantum chemistry*, Wiley, Chichester, West Sussex, 2003.
- (28) H. Hertz, *Annalen der Physik*, 1887, **267**, 983–1000.
- (29) A. Einstein, *Annalen der Physik*, 2005, **14**, 164–181.
- (30) A. K. Pradhan and S. N. Nahar, *Atomic astrophysics and spectroscopy*, Cambridge University Press, Cambridge, 2012.
- (31) D. W. Turner, *Philosophical Transactions of the Royal Society of London A: Mathematical, Physical and Engineering Sciences*, 1970, **268**, 7–31.
- (32) J. H. D. Eland, *Photoelectron spectroscopy : an introduction to ultraviolet photoelectron spectroscopy in the gas phase*, Elsevier Ltd, London, 2nd, 1984.
- (33) T. Koopmans, *Physica*, 1934, **1**, 104–113.
- (34) M. Weissbluth, *Atoms and molecules*, Academic Press, New York, 1st, 1978.

BIBLIOGRAPHY

- (35) C. F. Brucker, *Electron spectroscopy: Theory, techniques and applications*, ed. C. R. Brundle and A. D. Baker, Academic Press, London, 1982, vol. 4.
- (36) D. C. Harris, *Symmetry and spectroscopy : an introduction to vibrational and electronic spectroscopy*, Oxford University Press, New York, 1978.
- (37) A. Corney, *Atomic and Laser Spectroscopy*, Oxford University Press, Oxford, UK, 2007, pp. 1–784.
- (38) C. J. Foot, *Atomic Physics*, Oxford University Press, Oxford, UK, 2004.
- (39) U. Becker and D. A. Shirley, *VUV and Soft X-Ray Photoionization*, ed. U. Becker and D. A. Shirley, Springer, Boston, MA, 1996.
- (40) C. L. Briant and R. P. Messmer, *Auger electron spectroscopy*, Academic Press, New York, 1988, pp. 1–259.
- (41) S. Hofmann, *Auger- and X-Ray Photoelectron Spectroscopy in Materials Science*, Springer, Berlin, Heidelberg, 2013.
- (42) J. A. van Bokhoven and C. Lamberti, *X-Ray Absorption and X-Ray Emission Spectroscopy: Theory and Applications*, Wiley Online Library, Chichester, West Sussex, 2015, vol. 1-2, pp. 1–845.
- (43) B. Fain and P. W. Milonni, *Journal of the Optical Society of America B*, 1987, **4**, 78.
- (44) H. Sato, *Chemical Reviews*, 2001, **101**, 2687–2726.
- (45) W. Demtröder, *Atoms, Molecules and Photons*, Springer, Berlin, Heidelberg, 2010.
- (46) S. Schlemmer, T. Giesen and H. Mutschke, *Laboratory astrochemistry : from molecules through nanoparticles to grains*, Wiley-VCH Verlag, Weinheim, Germany, 2015, pp. 1–531.
- (47) T. Baer, *International Journal of Mass Spectrometry*, 2000, **200**, 443–457.
- (48) C.-Y. Ng, *Vacuum Ultraviolet Photoionization and Photodissociation of Molecules and Clusters*, World Scientific Publishing, Singapore, 1991.
- (49) U. Becker and D. A. Shirley, *VUV and Soft X-Ray Photoionization*, Springer, Boston, MA, 1996.
- (50) F. Trinter, L. Schmidt, T. Jahnke, M. Schöffler, O. Jagutzki, A. Czausch, J. Lower, T. Isaev, R. Berger, A. Landers, T. Weber, R. Dörner and H. Schmidt-Böcking, *Molecular Physics*, 2012, **110**, 1863–1872.

BIBLIOGRAPHY

- (51) M. Takahashi, J. P. Cave and J. H. Eland, *Review of Scientific Instruments*, 2000, **71**, 1337–1344.
- (52) E. Kukk, R. Sankari, M. Huttula, A. Sankari, H. Aksela and S. Aksela, *Journal of Electron Spectroscopy and Related Phenomena*, 2007, **155**, 141–147.
- (53) J. Laskin and C. Lifshitz, *Journal of Mass Spectrometry*, 2001, **36**, 459–478.
- (54) P. Morin and C. Miron, *Journal of Electron Spectroscopy and Related Phenomena*, 2012, **185**, 259–266.
- (55) O. Travnikova, V. Kimberg, R. Flammini, X. J. Liu, M. Patanen, C. Nicolas, S. Svensson and C. Miron, *Journal of Physical Chemistry Letters*, 2013, **4**, 2361–2366.
- (56) R. E. Continetti, *Annual Review of Physical Chemistry*, 2001, **52**, 165–192.
- (57) T. Baer, *Encyclopedia of Spectroscopy and Spectrometry*, 1999, 1831–1839.
- (58) J. Larmor, *The London, Edinburgh, and Dublin Philosophical Magazine and Journal of Science*, 1897, **44**, 503–512.
- (59) F. R. Elder, A. M. Gurewitsch, R. V. Langmuir and H. C. Pollock, *Physical Review*, 1947, **71**, 829–830.
- (60) S. Mobilio, F. Boscherini and C. Meneghini, *Synchrotron Radiation Basics, Methods and Applications*, Springer-Verlag, Berlin, Heidelberg, 2016.
- (61) A. Balerna and S. Mobilio, in *Synchrotron Radiation*, Springer, Berlin, Heidelberg, 2015, pp. 3–28.
- (62) S. P. Cramer, *X-ray spectroscopy with synchrotron radiation : fundamentals and applications*, Springer International Publishing, Cham, 1st, 2020.
- (63) X. Zhang, *Synchrotron radiation applications*, World Scientific Publishing, Singapore, 2018.
- (64) D. Olsson, Ph.D. Thesis, Lund University, 2017, pp. 1–216.
- (65) G. Shenoy, *Structural Chemistry*, 2003, **14**, 3–14.
- (66) H. Stuhrmann, *Angewandte Chemie*, 1989, **101**, 651–652.
- (67) *Undulator* - Wikipedia <https://en.wikipedia.org/wiki/Undulator> (Accessed: 25-02-2020).
- (68) *Undulators, wigglers and their applications*, ed. H Onuki and P Elleaume, Taylor & Francis Group, London, 1st, 2003.

BIBLIOGRAPHY

- (69) R. Pärna, R. Sankari, E. Kukk, E. Nõmmiste, M. Valden, M. Las-tusaari, K. Kooser, K. Kokko, M. Hirsimäki, S. Urpelainen, P. Tu-runen, A. Kivimäki, V. Pankratov, L. Reisberg, F. Hennies, H. Tarawneh, R. Nyholm and M. Huttula, *Nuclear Instruments and Methods in Physics Research Section A: Accelerators, Spectrometers, Detectors and Associated Equipment*, 2017, **859**, 83–89.
- (70) K. Kooser, A. Kivimäki, P. Turunen, R. Pärna, L. Reisberg, M. Kirm, M. Valden, M. Huttula and E. Kukk, *Journal of Synchrotron Radia-tion*, 2020, **27**, 1080–1091.
- (71) *Model 3076 Constant Output Atomizer Instruction Manual*, TSI Inc, Minnesota, United States.
- (72) *Model 3062 Diffusion Dryer Instruction Manual*, TSI Inc., Minnesota, United States.
- (73) M. Faubel, S. Schlemmer and J. P. Toennies, *Zeitschrift für Physik D Atoms, Molecules and Clusters*, 1988, **10**, 269–277.
- (74) K. R. Wilson, B. S. Rude, J. Smith, C. Cappa, D. T. Co, R. D. Schaller, M. Larsson, T. Catalano and R. J. Saykally, *Review of Sci-entific Instruments*, 2004, **75**, 725–736.
- (75) C. Nordling, E. Sokolowski and K. Siegbahn, *Physical Review*, 1957, **105**, 1676–1677.
- (76) D. W. Turner and M. I. Jobory, *The Journal of Chemical Physics*, 1962, **37**, 3007–3008.
- (77) K. Siegbahn, *Philosophical Transactions of the Royal Society of Lon-don. Series A, Mathematical and Physical Sciences*, 1970, **268**, 33–57.
- (78) Scienta Omicron - <https://www.scientaomicron.com/en/home> (Ac-cessed: 02-12-2019).
- (79) M. Huttula, S. Heinäsmäki, H. Aksela, E. Kukk and S. Aksela, *Jour-nal of Electron Spectroscopy and Related Phenomena*, 2007, **156–158**, 270–273.
- (80) B. A. Mamyrin, *International Journal of Mass Spectrometry*, 2001, **206**, 251–266.
- (81) W. C. Wiley and I. H. McLaren, *Review of Scientific Instruments*, 1955, **26**, 1150–1157.
- (82) N. Mirsaleh-Kohan, W. D. Robertson and R. N. Compton, *Mass Spec-trometry Reviews*, 2008, **27**, 237–285.

BIBLIOGRAPHY

- (83) O. Jagutzki, A. Cerezo, A. Czasch, R. Dörner, M. Hattaß, M. Huang, V. Mergel, U. Spillmann, K. Ullmann-Pfleger, T. Weber, H. Schmidt-Böcking and G. D. Smith, *IEEE Transactions on Nuclear Science*, 2002, **49 II**, 2477–2483.
- (84) D. C. Koningsberger and R. Prins, *X-ray absorption : principles, applications, techniques of EXAFS, SEXAFS, and XANES*, Wiley, New York, 1988.
- (85) *EXAFS Spectroscopy*, ed. B. K. Teo and D. C. Joy, Springer-Verlag, Boston, MA, 1981.
- (86) J. Stohr, *NEXAFS Spectroscopy*, Springer, Berlin, Heidelberg, 2003.
- (87) T. A. Carlson, *Photoelectron and Auger spectroscopy*, Springer-Verlag, Boston, MA, 2013.
- (88) P. M. A. Sherwood, *Analytical and Bioanalytical Chemistry*, 2013, **405**, 2415–2416.
- (89) D. Betteridge, *International Journal of Environmental Analytical Chemistry*, 1972, **1**, 243–257.
- (90) H. E. De and S. Vincent, *Mass Spectrometry: principles and applications*, Wiley, Somerset, 3rd, 2013.
- (91) J. T. Watson and O. D. Sparkman, *Introduction to Mass Spectrometry: Instrumentation, Applications and Strategies for Data Interpretation*, John Wiley and Sons, Somerset, 4th, 2013.
- (92) J. H. Eland, F. S. Wort and R. N. Royds, *Journal of Electron Spectroscopy and Related Phenomena*, 1986, **41**, 297–309.
- (93) L. J. Frasinski, M. Stankiewicz, K. J. Randall, P. A. Hatherly and K. Codling, *Journal of Physics B: Atomic and Molecular Physics*, 1986, **19**, L819.
- (94) *Chemical Applications of Synchrotron Radiation*, ed. T.-K. Sham, World Scientific Publishing, Singapore, 2002, vol. 12.
- (95) P. A. Hatherly, M. Stankiewicz, L. J. Frasinski, K. Codling and M. A. MacDonald, *Chemical Physics Letters*, 1989, **159**, 355–360.
- (96) M. Simon, M. Lavollée, M. Meyer and P. Morin, *Journal of Electron Spectroscopy and Related Phenomena*, 1996, **79**, 401–406.
- (97) J. H. Eland, F. S. Wort, P. Lablanquie and I. Nenner, *Zeitschrift für Physik D Atoms, Molecules and Clusters*, 1986, **4**, 31–42.
- (98) E. Itälä, D. T. Ha, K. Kooser, E. Nömmiste, U. Joost and E. Kukk, *International Journal of Mass Spectrometry*, 2011, **306**, 82–90.

BIBLIOGRAPHY

- (99) E. Itälä, E. Kukk, D. T. Ha, S. Granroth, A. Caló, L. Partanen, H. Aksela and S. Aksela, *Journal of Chemical Physics*, 2009, **131**, 114314.
- (100) E. Kukk, R. Sankari, M. Huttula, A. Sankari, H. Aksela and S. Aksela, *Journal of Electron Spectroscopy and Related Phenomena*, 2007, **155**, 141–147.
- (101) *CoboldPC (User Manual) - Roentdek Handels GmbH*, Kelkheim, Germany, 2011.
- (102) A. Lindgren, M. Gisselbrecht, F. Burmeister, A. Naves De Brito, A. Kivimäki and S. L. Sorensen, *Journal of Chemical Physics*, 2005, **122**, 114306.
- (103) D. T. Ha, M. A. Huels, M. Huttula, S. Urpelainen and E. Kukk, *Physical Review A - Atomic, Molecular, and Optical Physics*, 2011, **84**, 033419.
- (104) L. Inhester, B. Oostenrijk, M. Patanen, E. Kokkonen, S. H. Southworth, C. Bostedt, O. Travnikova, T. Marchenko, S. K. Son, R. Santra, M. Simon, L. Young and S. L. Sorensen, *Journal of Physical Chemistry Letters*, 2018, **9**, 1156–1163.
- (105) E. Itälä, H. Myllynen, J. Niskanen, J. González-Vázquez, Y. Wang, D. T. Ha, S. Denifl and E. Kukk, *Journal of Physical Chemistry A*, 2019, **123**, 3074–3079.
- (106) H. Levola, E. Itälä, K. Schlesier, K. Kooser, S. Laine, J. Laksman, D. T. Ha, E. Rachlew, M. Tarkanovskaja, K. Tanzer and E. Kukk, *Physical Review A - Atomic, Molecular, and Optical Physics*, 2015, **92**, 063409.
- (107) J. H. D. Eland, *Laser Chemistry*, Hindawi Limited, 1991, vol. 11, pp. 259–263.
- (108) M. Simon, T. Lebrun, R. Martins, G. G. De Souza, I. Nenner, M. Lavollee and P. Morin, *Journal of Physical Chemistry*, 1993, **97**, 5228–5237.
- (109) G. Prümper and K. Ueda, *Nuclear Instruments and Methods in Physics Research, Section A: Accelerators, Spectrometers, Detectors and Associated Equipment*, 2007, **574**, 350–362.
- (110) G. J. Mturi and B. S. Martincigh, *Journal of Photochemistry and Photobiology A: Chemistry*, 2008, **200**, 410–420.
- (111) M. Yamaji and M. Kida, *Journal of Physical Chemistry A*, 2013, **117**, 1946–1951.
- (112) S. Hsieh and J. H. Eland, *The Journal of Chemical Physics*, 1995, **103**, 1006–1012.

BIBLIOGRAPHY

- (113) S. MacLot, D. G. Piekarski, A. Domaracka, A. Méry, V. Vizcaino, L. Adoui, F. Martín, M. Alcamí, B. A. Huber, P. Rousseau and S. Díaz-Tendero, *Journal of Physical Chemistry Letters*, 2013, **4**, 3903–3909.
- (114) P. C. Chang, Y. Yu, Z. H. Wu, P. C. Lin, W. R. Chen, C. C. Su, M. S. Chen, Y. L. Li, T. P. Huang, Y. Y. Lee and C. C. Wang, *Journal of Physical Chemistry B*, 2016, **120**, 10181–10191.
- (115) O. Kostko, B. Xu, M. I. Jacobs and M. Ahmed, *Journal of Chemical Physics*, 2017, **147**, 013931.

Abdul Rahman Abid

2021

ISBN 978-952-62-2884-6 (Printed)

ISBN 978-952-62-2885-3 (PDF)

ISSN 1239-4327